Multiwavelength observations of MAXI J1820+070 during its outburst decay and subsequent mini-outburst

M. Özbey Arabacı[1]*, E. Kalemci[2], T. Dinçer[3], C. D. Bailyn[3], D. Altamirano[1], T. Ak[4],

[1]*Department of Physics and Astronomy, University of Southampton, Southampton, SO17 1BJ, UK*
[2]*Faculty of Engineering and Natural Sciences, Sabancı University, Orhanlı-Tuzla, 34956 Istanbul, Turkey*
[3]*Department of Astronomy, Yale University, PO Box 208101, New Haven, CT 06520-8101, USA*
[4]*Istanbul University, Faculty of Science, Department of Astronomy and Space Sciences, 34119, Istanbul, Turkey*

ABSTRACT

We present results from quasi-simultaneous multiwavelength observations of the Galactic black hole X-ray transient MAXI J1820+070 during the decay of the 2018 outburst and its entire subsequent mini-outburst in March 2019. We fit the X-ray spectra with phenomenological and Comptonizaton models and discuss the X-ray spectral evolution comparing with the multiwavelength behaviour of the system. The system showed a rebrightening in UV/Optical/NIR bands 7-days after the soft-to-hard transition during the main outburst decay while it was fading in X-rays and radio. In contrast, the mini-outburst occurred 165-days after the hard state transition of the initial outburst decay and was detected in all wavelengths. For both events, the measured timescales are consistent with those observed in other black hole systems. Contemporaneous hard X-ray/soft γ-ray observations indicate a non-thermal electron energy distribution at the beginning of the UV/Optical/NIR rebrightening, whereas a thermal distribution can fit the data during the hard mini-outburst activity. The broadband spectral energy distributions until the rebrightening are consistent with the irradiated outer accretion disc model. However, both the SEDs produced for the peak of rebrightening and close to the peak of mini-outburst provided good fits only with an additional power-law component in the UV/Optical/NIR frequency ranges which is often interpreted with a jet origin.

Key words: stars: black holes – stars: individual: MAXI J1820+070 – X-rays: binaries

1 INTRODUCTION

Galactic black hole transient (GBHT) systems spend most of their time in a faint, quiescent state where mass transfer rate from the accretion disc onto the black hole is at a very low level (Tanaka & Lewin 1995; McClintock & Remillard 2006). Occasionally, they become active and undergo weeks to months long transient outbursts (Tanaka & Shibazaki 1996; Dunn et al. 2010; Reynolds & Miller 2013; Corral-Santana et al. 2016; Tetarenko et al. 2016) due to rapid and dramatic increase in mass accretion rate driven by the thermal-viscous instabilities developing in the disc (Meyer & Meyer-Hofmeister 1981; Coriat et al. 2012, and references therein). During these outbursts, the GBHTs often follow a similar evolutionary track through a sequence of different X-ray states depending on their temporal and spectral properties. In general, a typical GBHT outburst starts in the hard state, make a transition to the soft state and eventually returns to the hard state at the end of the outburst (see Remillard & McClintock 2006; Belloni 2010; Belloni & Motta 2016, for reviews). In addition, during the transitions between the hard and soft states, the GBHT may go through several intermediate states displaying a cyclic 'q-shaped' pattern in the hardness-intensity diagram (HID) in which the X-ray luminosity is plotted versus spectral hardness (Homan et al. 2001; Maccarone 2003; Belloni et al. 2005).

In the hard state, the X-ray spectrum of a GBHT is dominated by a hard power-law component with a high energy cut-off broadly associated with the Comptonization of soft photons in a hot ($kT_e \sim 100$ keV), optically thin electron corona or hot inner flow (Sunyaev & Truemper 1979; Poutanen 1998; Gilfanov 2010; Zdziarski & Gierliński 2004). The contribution from the optically thick regions to the X-ray emission in this state is very weak and generally interpreted as the truncation of the inner disc to be far away from the innermost stable circular orbit (ISCO, Esin et al. 1997; Poutanen et al. 1997). By contrast, the inner disc radius may extend down or close to the ISCO in the soft state. The X-ray spectrum is characterized by a thermal, blackbody component peaking at ∼1 keV accompanied with a weak hard power-law tail extending well beyond the γ-ray regime without a break. The soft X-ray component is associated with a standard optically thick and geometrically thin accretion disc (Shakura & Sunyaev 1973) whereas the physical origin of the non-thermal high energy tail is still not clear (see Cangemi et al. 2021, for the application of different models for Cyg X-1). During the transitional intermediate states, the source spectrum is more compare to the main two states and includes both hard power-law emission from the corona/hot flow and soft thermal emission from the accretion disc (see Remillard & McClintock 2006, and the references therein for the details of intermediate states and state transitions)

* E-mail: m.ozbey-arabaci@soton.ac.uk

Multiwavelength monitoring of GBHTs have revealed that changes in the radio and optical-infrared (OIR) emission properties are closely related to the X-ray spectral states (Fender et al. 2009; Corbel et al. 2000; Vadawale et al. 2003; Homan et al. 2005; Dinçer et al. 2012; Miller-Jones et al. 2012; Russell et al. 2012, 2019a; Kalemci et al. 2013; Fender & Gallo 2014; Carotenuto et al. 2021). In the hard state, the spectral energy distributions (SEDs) show a flat/slightly inverted synchrotron spectrum ($F_\nu \propto \nu^\alpha$, where the spectral index $\alpha \geqslant 0$) extending from radio to millimeter bands (Fender 2001; Tetarenko et al. 2015) and breaking to an optically thin emission ($\alpha < 0$) at the IR regime indicating a collimated and compact jet (Fender et al. 2001; Russell et al. 2006, 2013, 2014). Close to the transition to the hard-to-soft state, however, the compact jet switches off and the radio emission is quenched below the detection levels in the soft state (Fender et al. 1999; Gallo et al. 2003; Russell et al. 2019a; Carotenuto et al. 2021). Following the transition back to the hard state at the outburst decay, the compact jet reforms progressively as indicated by the evolution in the radio flux, radio spectral index and IR-optical SEDs (Miller-Jones et al. 2012; Kalemci et al. 2013; Corbel et al. 2013; Russell et al. 2014). Also in the OIR regime, correlations between X-ray and OIR flux have been determined (Homan et al. 2005; Coriat et al. 2009). This led to the discussion of possible X-ray emission mechanisms in the hard state other than thermal Comptonization, such as direct synchrotron (Markoff et al. 2001; Russell et al. 2010) and/or synchrotron self-Compton radiation (Markoff et al. 2005) suggesting the jet could make significant contribution to the high frequency emission assuming that the hot electron corona as the base of the jet (Markoff et al. 2003). A plausible way to probe this contribution on the X-ray spectra could be achieved by invoking the models including non-thermal/hybrid electron distribution in the spectral fits as the jet provides non-thermal electrons into the corona and modifies the electron energies.

The GBHT outburst light curves could be very complicated, and while the so called "main outburst" could go through the spectral states described above, some GBHTs also show rebrightening episodes during the outburst decay Kalemci et al. (2013) and/or an increase in brightness several days after the X-ray flux goes below the detection limits of the most observatories that are sometimes defined as mini-outbursts (Chen et al. 1997). A systematic multiwavelength study of GBHTs in the outburst decay by Kalemci et al. (2013) showed that for most of the systems, a rebrightening (secondary maximum or secondary flare) in OIR occurred ∼ 1-2 weeks after the soft-to-hard transition. Detection of rebrightening during the outburst decay supports the argument that formation of compact jet and its interaction with the accretion environment are imprinted on the multiwavelength behaviour of the GBHTs (Buxton & Bailyn 2004; Buxton et al. 2012; Kalemci et al. 2005, 2013; Dinçer et al. 2012; Corbel et al. 2013). Alternatively, the synchrotron radiation from the hot accretion flow model (Poutanen 1998; Veledina et al. 2013), or the irradiation from the secondary star or outer part of the disc could explain the brightness increase in the OIR bands. In contrast, there are limited number of pointed hard X-ray observations for the mini-outbursts (e.g. XTE J1752−223, SWIFT J1745−26, and V404 Cyg, Chun et al. 2013; Kalemci et al. 2014; Muñoz-Darias et al. 2017) since they have been observed frequently in the soft X-rays and optical (see Chen et al. 1997 for some historical examples, both in black holes and neutron stars). A recent study by Zhang et al. (2019) attempted a classification of the rebrightenings during/after the main outburst decay based on the the available fluxes and applied this scheme to Swift J1753.5−0127 which showed a mini-outburst in radio, optical and X-rays. It can be seen that different flavors exist depending on whether the source reaches quiescence first. Some sources show multiple mini-outbursts after the initial outburst (e.g. XTE J1650−500, MAXI J1535−571 Tomsick et al. 2003; Cúneo et al. 2020). Although the origin of the mini-outbursts is still debated, an increased mass accretion triggered by the events during the evolution of the primary outburst through heating of the outer parts of the accretion disc (Ertan & Alpar 2002), or the companion star (Augusteijn et al. 1993) are known to be the likely explanations.

In this paper, we examine two such brightening episodes of MAXI J1820+070 that occurred close to the end of its main outburst decay in 2018 and the following post-outburst event in March 2019. Fig. 1 shows the long-term hard X-ray (15-50 keV) light curve of MAXI J1820+070 from the Burst Alert Telescope BAT onboard the *Neil Gehrels Swift Observatory* Gehrels et al. (2004) and corresponding HID (J. Wang, private communication, 2022) obtained from the *Neutron Star Interior Composition Explorer* (Gendreau et al. 2016, *NICER*). Previous works covering these episodes have used different classifications (e.g. rebrightening, brightening, flare, reflare or outburst) to signify the brightness increase in different wavelengths for MAXI J1820+070. Here, we refer to the flux increase in the hard X-ray (before the state transition) and the UV-optical-near IR bands (UOIR) in the main outburst decay (during the hard state) as rebrightening and the one between MJD 58555-58590 as mini-outburst to be consistent with Kalemci et al. (2013) and Zhang et al. (2019), respectively (see Fig. 1).

Determining the multiwavelength characteristics of GBHTs during and/or after the soft-to-hard transition at the final stages of the outburst is of great importance to disentangle the physical mechanisms governing these rebrightenings and understanding the conditions for the jet formation as well as the possible effects of jet on the X-ray spectral properties. Especially simultaneous and concurrent radio observations are extremely important as the origin of the optical emission can be originated from multiple sources, but the radio through infrared is generally established as being dominated by jet emission. Therefore, the work presented here mainly focuses on the hard state X-ray spectral properties and their evolution combined with multiwavelength information. Our data set includes quasi-simultaneous monitoring from *Swift*, the Small & Moderate Aperture Research Telescope System (SMARTS, Subasavage et al. 2010) and TÜBİTAK National Observatory (TUG) at X-ray, ultraviolet (UV), optical, and near-infrared (NIR) bands, together with *INTErnational Gamma-Ray Astrophysics Laboratory* (*INTEGRAL*, Winkler et al. 2003) data in soft γ-rays, two covering the main outburst decay and the other one close to the peak of the mini-outburst which never reached the soft state. We also make use of the radio data collected from the previous reports (Bright et al. 2018, 2020; Shaw et al. 2021) to discuss the jet formation with respect to the evolution of the source as the radio emission is the best indicative of jet evolution. We should point out that this is the first multiwavelength study of MAXI J1820+070 dedicated to discuss its multiwavelength behaviour extending to soft γ-ray regime (above 200 keV) at the main outburst decay as well as its subsequent mini-outburst. This paper is structured as follows: we introduce the source in Section 2 and describe in detail our observations and data reduction procedures in Section 3. Section 4 presents the results of multiwavelength spectral evolution and broadband spectra. Finally, we discuss the implications of the results in Section 5 and summarise them in Section 6.

2 MAXI J1820+070

The X-ray transient MAXI J1820+070 was discovered with the Monitor of All-Sky X-ray Image (MAXI) early in its outburst in

March 2018 (Kawamuro et al. 2018) and it was soon associated with an optical transient ASASSN-18ey detected by the All-Sky Automated Survey for Super-Novae (ASAS-SN) 5 days prior to the X-rays (Denisenko 2018). Subsequent follow-up observations revealed that the optical/X-ray flux ratio and the X-ray spectral properties of the source to be consistent with those of GBHTs in the hard state (Baglio et al. 2018a; Homan et al. 2018; Uttley et al. 2018). This classification has been cemented dynamically by Torres et al. (2019). The system includes a BH with a mass of $5.95^{0.39}_{0.22}$ $M_\odot$ and a K type companion (Torres et al. 2020) at a distance of 2.96±0.33 kpc (Atri et al. 2020).

A radio counterpart to the source was also detected with Arcminute Microkelvin Imager Large Array (AMI-LA) and the RATAN-600 telescope (Bright et al. 2018; Trushkin et al. 2018) during the initial hard state that lasted more than 3 months (Roques & Jourdain 2019; Shidatsu et al. 2018). Compact jet detection was reported by Bright et al. (2018) and subsequent radio observations revealed the discovery of a short-lived radio flare associated with the launch of bipolar superluminal ejections during the hard-to-soft state transition by (Bright et al. 2020). Homan et al. (2020) reported the switch between type-C to type-B quasi periodic oscillations (QPO) that might be linked to discrete ejections. These powerful ejection events were also detected in X-rays with *Chandra* (Espinasse et al. 2020). Using a new dynamic phase centre tracking technique on Very Long Baseline Array observations (VLBA) of the approaching fast moving ejecta, Wood et al. (2021) identified a previously undetected approaching slow-moving jet knot lasted for ~6 h. They showed that this slow component was responsible for the radio flare and for the QPO transition rather than the fast-moving ejecta stated in the previous works (Bright et al. 2020; Homan et al. 2020).

The source went through all canonical accretion states during the 2018 outburst and underwent rebrightening episodes during the outburst decay before fading into quiescence in X-rays (or extremely low X-ray luminosities) in November 2018 (Homan et al. 2020; Shidatsu et al. 2019, see also Fig. 1) though pre-outburst level in the optical band was reached ~2 months later (Russell et al. 2019b). After remaining in quiescence for ~3.5 months, the source experienced a weak (~ 30 mCrab in 2-4 keV band), 2-month long mini-outburst in March 2019 (Ulowetz et al. 2019; Bahramian et al. 2019; Vozza et al. 2019) and showed three more, relatively weak X-ray activities since then (Xu et al. 2019; Bright et al. 2019; Hankins et al. 2019; Adachi et al. 2020; Sasaki et al. 2020; Baglio et al. 2021; Homan et al. 2021; Sai et al. 2021).

3 MULTIWAVELENGTH OBSERVATIONS AND ANALYSIS

Figure 2 shows the soft X-ray (2-4 keV), hard X-ray (15-50 keV) and the UOIR band light curves of the outburst decay and the subsequent mini-outburst covered by MAXI/GSC (Miller et al. 2006), *Swift*/BAT (Barthelmy et al. 2005), SMARTS, and TUG telescopes. The soft and hard X-ray data are provided as daily averages by MAXI/GSC (Matsuoka et al. 2009) and *Swift*/BAT teams (Krimm et al. 2013). The dates of *INTEGRAL* pointing observations are marked with grey vertical lines. As it is also shown in Fig. 1, the source evolved from the soft to hard state during the rebrightening and remained in the hard state for the entire mini-outburst period.

3.1 Swift

We analysed a total of 47 *Swift* observations collected with the XRT (Burrows et al. 2005) and UVOT (Roming et al. 2005) instruments between 17 September 2018 and 4 April 2019. The observations were taken exclusively during the outburst decay and mini-outburst phases, with a cadence of every few days.

The XRT spectra were extracted using the standard HEASOFT v6.24 [1] with the 2018 July version of the HEASARC calibration database (CALDB). The first nine observations suffered from photon pile-up. To mitigate the pile-up problem, we limited our spectral extraction to the single pixel events and used an annulus region centred at the source location, excising the central pixels. More specifically, the inner radius of the annulus was set to the radius where the extracted count rate fell below 100 cts s^{-1} and the outer radius of the annulus was fixed at 70″ (30 pixels). Spectra from the pile-up free observations were extracted in the same manner but without excluding the central pixels. For the instrumental calibration, the appropriate response matrix file `swxwt0s6psf1_20131212v001.rmf` was obtained from HEASARC CALDB and auxiliary response files were created using `xrtmkarf` with the exposure map created by `xrtexpomap`. For model fitting, each spectrum was grouped to have at least one photon per spectral bin using `grppha`.

UVOT photometry was done using the `uvotsource` tool, which returns both the background-corrected magnitudes in the Vega system and the flux densities in mJy. The source counts were extracted from a circular region with an aperture radius of 5″ centred on the source and the background counts were done from a source-free, circular region with a radius of 10″.

3.2 INTEGRAL

We observed MAXI J1820+070 with JEM-X (Lund et al. 2003), IBIS Soft Gamma-Ray Imager (ISGRI, Lebrun et al. 2003), and SPI (Vedrenne et al. 2003) instruments onboard the *INTEGRAL* satellite during the revolutions of 2006, 2007, and 2072. The data were processed using the Off-line Scientific Analysis (`OSA`) software version 11.0 provided by the *INTEGRAL* Science Data Centre (ISDC; Courvoisier et al. 2003). The standard extraction algorithm was used to obtain JEM-X and IBIS/ISGRI spectra for each revolution. JEM-X spectra were extracted for an energy range of 3–35 keV corresponding to 16 channels while IBIS/ISGRI spectra were produced to have 53 energy bins in 30–350 keV band. In order to have optimum simultaneity with the *Swift* observations within the revolution, we split the extracted spectra into five segments (see Table 1). The average spectrum of each group has been obtained through `spe_pick` tool to get a better signal to noise ratio. In this work we considered only JEM-X1 and IBIS/ISGRI instruments as JEM-X1 provided better statistics than JEM-X2 and SPI did not yield a source detection above 200 keV.

3.3 SMARTS & TUG

As part of our SMARTS X-ray binary program, we observed MAXI J1820+070 on a near-daily basis in the second half of 2018 October as well as between 2019 March 21 and 2019 May 2. The observations were taken with the ANDICAM[2] instrument (DePoy et al. 2003) on the SMARTS 1.3-m telescope at the Cerro Tololo Inter-American Observatory (CTIO) using the standard KPNO Johnson-Cousin optical *BVI* filters and standard CIT/CTIO *JHK* filters for the NIR. A nightly observing sequence consisted of several exposures in each of

---

[1] https://www.swift.ac.uk/analysis/xrt/spectra.php
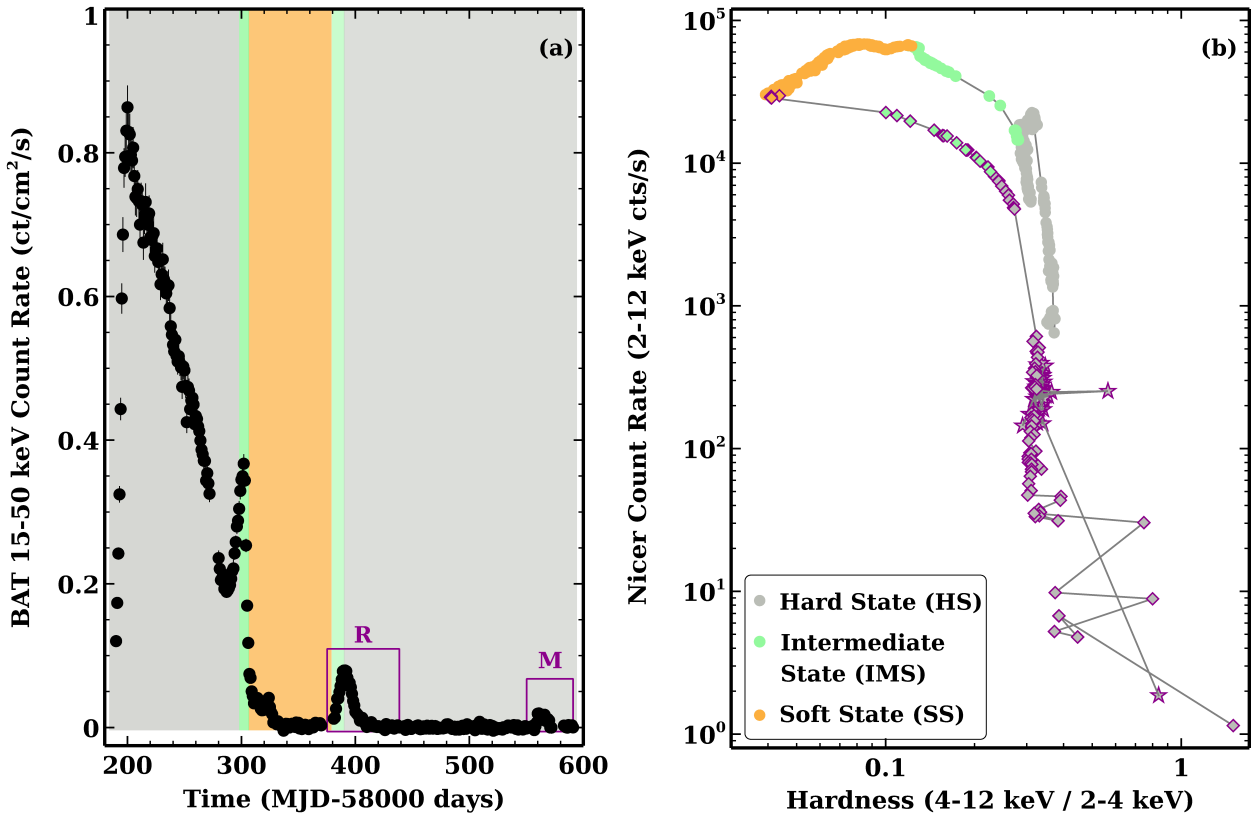[2] https://www.astronomy.ohio-state.edu/ANDICAM/detectors.html, for further information about the instrument.

Figure 1: (a) *Swift*/BAT light curve of MAXI J1820+070 covering the full outburst started in March 2018. The rebrightening (R) and mini-ouburst (M) epochs studied in this work are highlighted with purple boxes. Coloured areas represent the spectral states of the source and match with the HID produced from NICER data (J. Wang, private communication, 2022) in panel (b). The day coincident with the *Swift*/XRT observations for the rebrightening and the mini-outburst events are denoted with the diamonds and stars in purple, respectively.

Table 1. Details of *INTEGRAL* observations.

Obs. No	ObsID	Revolution (MJD-58000)	Start-End Date (ks)	ISGRI Exposure	*Swift* ObsID
(1)	(2)	(3)	(4)	(5)	(6)
1	15400050001	2006	393.62-394.01	20.3	00010627106
2	15400050001	2006	394.01-395.00	51.6	00010627107
3	15400050001	2007	395.45-396.03	28.2	00010627108
4	15400050001	2007	397.01-397.65	33.4	00010627109
5	15400050001	2072	568.26-570.50	103.92	00010627149

Column (1): Observation number assigned for the *INTEGRAL* and *Swift* observations matched. Column (2): Observation ID. Column (3): *INTEGRAL* revolution. Column (4): Start and end date of *INTEGRAL* observations (MJD-58000 days). Column (5): Effective exposure time simultaneous with *Swift* observations. Column (6): *Swift* observation ID within the given observing time.

the optical bands and seven dithered exposures in each of the infrared bands. The exposure times were 30 s in V, 50 s in I and B, and 30 s in each of the dithered infrared images. We reduced all of the data in IRAF (Tody 1986, 1993) following the standard procedures described in Buxton et al. (2012). We performed point spread function photometry on all reduced images with the DAOPHOT4 suite of programs (Stetson 1987), and then converted the magnitudes to the Vega system with respect to four nearby field stars, with absolute calibration via the standard stars in the RU 149 field (Landolt 1992) on clear nights and the Two Micron All-Sky Survey catalog (Skrutskie et al. 2006) in optical and NIR. We also observed the source in optical bands with the T100 telescope at TUG through our DDT and TOO programs. These observations were taken on nine nights between

2018 September 28 and October 29 UT with exposure times of 60 s in B and V, and 40 s in R and I[3]. We extracted the source magnitudes from T100 images in the same way we did from the SMARTS images.

[3] See Table A3 and Table A2 for the effective wavelengths of the filters.
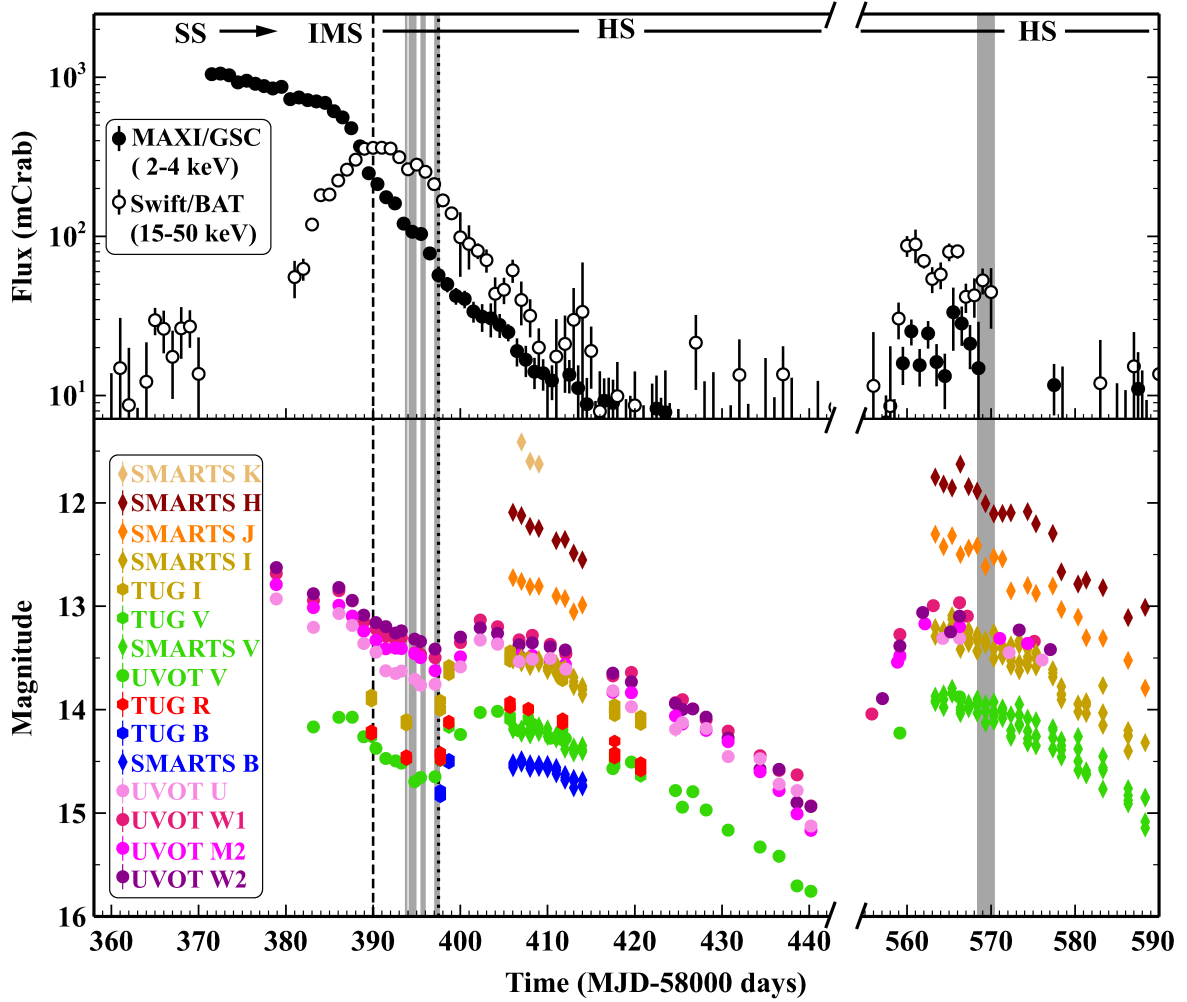
Figure 2: Multiwavelength light curves of MAXI J1820+070 during the rebrightening event in 2018 outburst decay (MJD 58360-58440) and the subsequent mini-outburst in 2019 (MJD 58555-58390). Dashed line separates the intermediate-to-hard state transition. Dotted line shows the onset of the rebrightening in UOIR band. Grey strips show the time of our *INTEGRAL* observations given in Table 1. Note that space between Obs.1 and Obs.2 is added for the clarity. The break in the time axis corresponds to a gap of ~110 days when the source was mainly in the quiescent state.

4 RESULTS

4.1 Multiwavelength Light Curves

Figure 2 presents the multiwavelength light curves of the main outburst decay and the mini-ouburst. The morphology of the hard X-ray and UOIR light curves are different for these two epochs. The rebrightening shows itself first in the hard X-rays between MJD 58380-58390. Afterwards, the UOIR band rebrightening occurs lasting until MJD 58440 while the hard X-ray flux drops. The mini-outburst, on the other hand, exhibits an increase in all bands after MJD 58555.

Determining the onset date of the rebrightening in the UOIR light curve is important as it allows investigation of associated changes in X-ray spectral and timing characteristics of the source around the same time for possible connections (Kalemci et al. 2013; Dinçer et al. 2014). We were able to constrain the onset of the rebrightening with a higher precision using the method described in Appendix A.3. of Kalemci et al. (2013). Thanks to the cadence of UVOT observations, we had a superior coverage between MJD 58390 and 58403 compared to the previous reports (Baglio et al. 2018b) and we were able to fit before and during transition points with much

smaller errors whereas Shidatsu et al. 2019 relies on g' data with a large gap of points before the transition. We found that the rebrightening in V-band started on MJD 58397.5 ± 0.5 day, a week after the hard state transition as shown in the next section.

We also note a possible rebrightening in the 10-20 keV band with MAXI between MJD 58402 and MJD 58410, almost coinciding with the UOIR peak. However, we cannot validate the statistical significance of this increase (adding a Gaussian peak to an exponentially decaying light curve provided a 0.10 chance probability with F-test). We only note that such increases in the hard X-rays are observed in GBHTs for those sources followed with pointed observations (Kalemci et al. 2013).

Finally it is worth comparing the evolution in radio to the evolution in UOIR (see Figs. 2 and 3). The radio flux increases after the initial measurement on MJD 58385.6 with AMI-LA (Bright et al. 2018) until MJD 58398, after which it starts to decrease with the X-ray flux. There is a delay of ~ 7-day between the compact radio peak and the UOIR band peak. No radio data has been reported covering the mini-outburst.
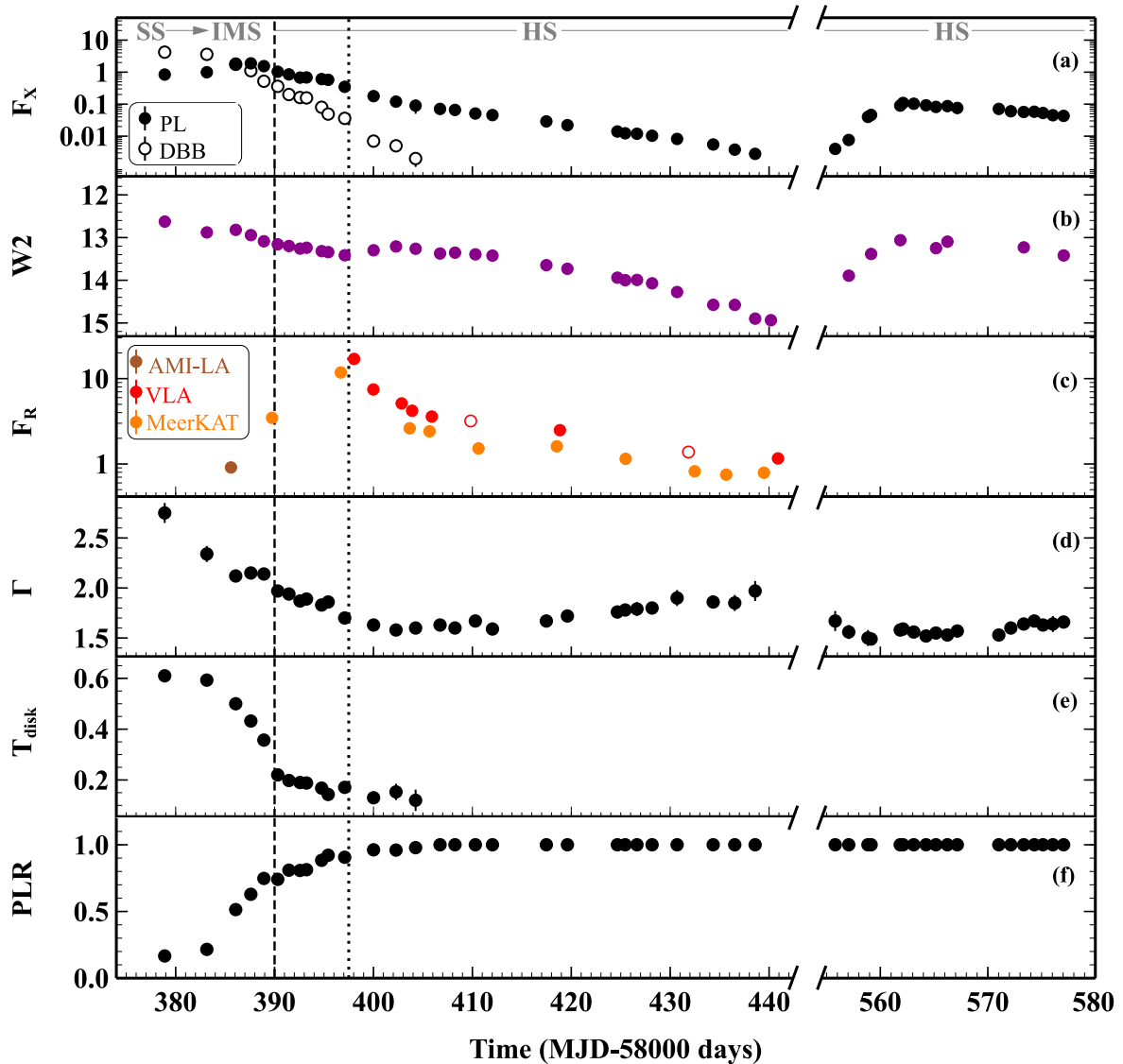
Figure 3: Evolution of (a) the power-law and disc blackbody fluxes in the 0.5-10 keV energy range in units of 10^{-8} erg s^{-1} cm^{-2}, (b) the W2 magnitude, (c) flux densities at 1.28 GHz (MeerKAT), 6 GHz (VLA) and at 15.5 GHz (AMI-LA) in units of mJy, (d) the photon index of the power-law, (e) the disc inner temperature in keV, and (f) the ratio of the power-law flux to the total flux in the 0.5-10 keV band. The dashed and dotted lines match those in Fig. 2. For the radio observations; two VLA data points represented in open circles are taken from Shaw et al. (2021), one AMI-LA detection obtained from Bright et al. (2018), and the rest are from Bright et al. (2020)
.

4.2 Spectral Results

All spectral analysis in the following subsections was performed using XSPEC v12.10.0c (Arnaud 1996). We took into account the Galactic absorption using the Tuebingen-Boulder absorption model (a.k.a. `tbabs`, Wilms et al. 2000) with the abundances of Wilms et al. (2000) and the cross sections of Verner et al. (1996). We also used a systematic errors of 3 and 1 per cent in the fits for data from the JEM-X and ISGRI instruments, . All quoted uncertainties are at the 90% confidence level unless otherwise stated.

4.2.1 Multiwavelength Evolution: Spectral States

We performed spectral fitting on the XRT data first to inspect the X-ray states of the source during its main outburst decay and the

mini-outburst. To do this, we used a composite model consisting of a standard disc blackbody (`diskbb`, Mitsuda et al. 1984) and a `power law`. The model described most of the spectra very well but over-fit the faint ones taken with short exposures, and in return yielded largely unconstrained parameters if the N_H values were kept free. In order to constrain the parameters better at all times, we first considered only the first four observations in our data set as they had the highest signal to noise ratio. The best-fit N_H values from these observations were statistically consistent with each other around a mean of $(1.2 \pm 0.3) \times 10^{21}$ cm^{-2} or a color excess of E(B-V) = 0.16 ± 0.05 (via Eq. 15 in Zhu et al. 2017). Having additional support from the fact that this color excess is consistent with the color excess of E(B-V) = 0.218 ± 0.003 reported in Schlafly & Finkbeiner (2011), we fixed the N_H at our average value and performed the fits again. The resulting best-fit parameters are shown in Table 2.

Table 2. Best-fit `tbabs × (diskbb + power law)` parameters obtained from the *Swift*/XRT spectral analysis, fixing N_H at 1.2×10^{21} atom cm^{-2}

Obs. Id	Start Time (MJD, UTC)	T_{disk} (keV)	Γ	F_{disk} (10^{-8} cgs)	F_{PL} (10^{-8} cgs)	W-stat/dof
(1)	(2)	(3)	(4)	(5)	(6)	(7)
00010627097	58378.89	0.610 ± 0.007	2.75 ± 0.10	4.21 ± 0.07	0.84 ± 0.08	1.00
00010627098	58383.15	0.593 ± 0.007	2.34 ± 0.08	3.60 ± 0.06	0.99 ± 0.07	1.02
00010627100	58386.07	0.500 ± 0.009	2.12 ± 0.04	1.75 ± 0.06	1.85 ± 0.07	1.00
00010627101	58387.60	0.432 ± 0.008	2.15 ± 0.04	1.11 ± 0.05	1.88 ± 0.06	0.99
00088657010	58388.92	0.357 ± 0.005	2.14 ± 0.02	0.52 ± 0.03	1.54 ± 0.03	1.24
00010627102	58390.32	0.220 ± 0.005	1.97 ± 0.03	0.36 ± 0.02	1.03 ± 0.02	1.07
00010627104	58391.45	0.198 ± 0.005	1.94 ± 0.02	0.20 ± 0.01	0.85 ± 0.01	1.07
00010627105	58392.57	0.190 ± 0.005	1.87 ± 0.02	0.161 ± 0.008	0.675 ± 0.007	1.17
00010627106	58393.23	0.188 ± 0.006	1.89 ± 0.03	0.157 ± 0.008	0.683 ± 0.008	1.06
00010627107	58394.76	0.168 ± 0.011	1.83 ± 0.03	0.080 ± 0.008	0.607 ± 0.008	1.06
00010627108	58395.42	0.143 ± 0.009	1.86 ± 0.02	0.049 ± 0.004	0.575 ± 0.004	1.20
00010627109	58397.09	0.171 ± 0.021	1.70 ± 0.04	0.036 ± 0.003	0.348 ± 0.003	0.95
00010627110	58400.01	0.130 ± 0.022	1.63 ± 0.03	0.007 ± 0.002	0.178 ± 0.003	0.95
00010627111	58402.28	0.153 ± 0.032	1.58 ± 0.04	0.005 ± 0.001	0.120 ± 0.002	1.08
00010627112	58404.26	0.120 ± 0.042	1.60 ± 0.03	0.0020 ± 0.0009	0.09 ± 0.04	0.98
00010627113	58406.73	-	1.63 ± 0.02	-	0.071 ± 0.001	0.98
00010627114	58408.24	-	1.60 ± 0.02	-	0.066 ± 0.001	0.92
00010627115	58410.30	-	1.67 ± 0.03	-	0.051 ± 0.001	1.10
00010627116	58412.03	-	1.59 ± 0.02	-	0.0455 ± 0.0009	0.97
00010627119	58417.48	-	1.67 ± 0.02	-	0.0289 ± 0.0004	0.91
00010627120	58419.61	-	1.72 ± 0.02	-	0.0221 ± 0.0003	0.95
00010627122	58424.66	-	1.76 ± 0.04	-	0.0140 ± 0.0005	0.92
00010627123	58425.45	-	1.78 ± 0.05	-	0.0123 ± 0.0005	0.87
00010627124	58426.64	-	1.79 ± 0.07	-	0.0119 ± 0.0006	0.85
00010627125	58428.17	-	1.80 ± 0.04	-	0.0103 ± 0.0003	0.95
00010627126	58430.70	-	1.90 ± 0.08	-	0.0082 ± 0.0004	0.97
00010627128	58434.35	-	1.86 ± 0.06	-	0.0055 ± 0.0003	0.90
00010627129	58436.53	-	1.85 ± 0.08	-	0.0038 ± 0.0002	0.94
00010627130	58438.59	-	1.97 ± 0.10	-	0.0028 ± 0.0002	0.93
00010627136	58555.80	-	1.67 ± 0.10	-	0.0040 ± 0.0003	0.86
00010627139	58557.06	-	1.56 ± 0.07	-	0.0076 ± 0.0005	0.89
00010627140	58558.85	-	1.50 ± 0.08	-	0.040 ± 0.003	0.94
00010627141	58559.14	-	1.49 ± 0.05	-	0.046 ± 0.002	0.93
00010627143	58561.85	-	1.58 ± 0.02	-	0.090 ± 0.002	1.03
00010627144	58562.11	-	1.59 ± 0.02	-	0.109 ± 0.002	0.98
00010627145	58563.11	-	1.56 ± 0.02	-	0.103 ± 0.002	1.07
00010627146	58564.25	-	1.52 ± 0.02	-	0.092 ± 0.002	0.98
00010627147	58565.17	-	1.55 ± 0.02	-	0.082 ± 0.002	0.93
00010627148	58566.24	-	1.53 ± 0.02	-	0.087 ± 0.001	1.04
00010627149	58567.16	-	1.57 ± 0.02	-	0.076 ± 0.001	1.00
00010627150	58571.02	-	1.53 ± 0.03	-	0.071 ± 0.002	0.95
00010627151	58572.14	-	1.60 ± 0.03	-	0.060 ± 0.001	0.99
00010627152	58573.34	-	1.64 ± 0.03	-	0.057 ± 0.001	1.01
00010627153	58574.32	-	1.67 ± 0.03	-	0.058 ± 0.001	1.08
00010627154	58575.13	-	1.63 ± 0.03	-	0.053 ± 0.001	0.90
00010627155	58576.05	-	1.64 ± 0.08	-	0.045 ± 0.003	0.90
00010627156	58577.05	-	1.66 ± 0.04	-	0.043 ± 0.001	0.81

Column (1): Observation Id. Column (2): Observation start time (MJD = JD-2400000.5). Column (3): disc inner temperature. Column (4): Photon index of the power-law. Column (5): disc flux in the 0.5-10 keV band. (6): Power-law flux in the 0.5-10 keV band. Column (7): Ratio of W-statistic to degrees of freedom. Errors on the fit parameters refer to the 1σ uncertainties.

Figure 3 presents the evolution of the X-ray spectral properties together with the U-band and the radio light curves of MAXI J1820+070. During the rise of the rebrightening in hard X-rays, between MJD 58378 and 58390, the spectra are generally soft with a mean photon index of 2.3 but a prominent change between the disc and the power-law components is also seen. In particular, the disc temperature decreases and the power-law flux peaks on MJD 58387.6. These changes indicate that the source was in transition

from the soft-to-intermediate state. Note that we are not able to distinguish sub-intermediate states as we do not have fast X-ray timing information. However, in the following days, the source became detectable in the radio with a flux density of 3.47 mJy at 1.28 GHz (Bright et al. 2020) followed by a sharp drop both in the spectral index and the disc temperature on MJD 58390. We mark this date as the transition from the intermediate-to-hard state, after which the power-law component starts to dominate the spectrum substantially.

Table 3. Best-fit `highecut × power law` parameters obtained from the XRT + JEM-X + ISGRI spectral analysis

Obs No	C_{JEM-X}	C_{ISGRI}	T_{disk} (keV)	Γ	E_{fold} (keV)	E_{cut} (keV)	Flux (10^{-8} cgs)	$\chi^2(\nu)$
(1)	(2)	(3)	(4)	(5)	(6)	(7)	(8)	(9)
1	0.78 ± 0.02	1.05 ± 0.06	0.200 ± 0.005	1.79 ± 0.02	154^{+56}_{-39}	99.79 ± 9.60	2.18 ± 0.02	1.23 (552)
2	0.81 ± 0.02	0.99 ± 0.06	0.197 ± 0.009	1.74 ± 0.02	199^{+34}_{-29}	84.13 ± 6.33	1.99 ± 0.02	1.32 (445)
3	0.75 ± 0.02	1.15 ± 0.06	0.167 ± 0.008	1.80 ± 0.02	136^{+64}_{-50}	117.32 ± 12.81	1.83 ± 0.02	1.53 (589)
4	0.92 ± 0.03	1.13 ± 0.06	0.175 ± 0.008	1.70 ± 0.02	219^{+63}_{-46}	83.13 ± 8.50	1.37 ± 0.01	1.00 (571)
5	0.84 ± 0.04	0.83 ± 0.06	-	1.60 ± 0.02	202^{+182}_{-81}	$<103^{\dagger}$	0.29 ± 0.01	1.08 (327)

Column (1): Observation number. Column (2-3): Energy independent cross-instrument normalization factors for the JEM-X and ISGRI, . C_{XRT} was frozen at 1. Column (4): disc inner temperature in units of keV. Column (5): Photon index (Γ) of the power-law. Column (6): Folding energy in the highecut model. Column (7): Cut off energy in the highecut model. Column (8): 0.5-350 keV unabsorbed flux in units of 10^{-8} erg cm^{-2} s^{-1}. Column (9): Reduced χ^2 for ν degree of freedom.
† 3σ upper limit.

Table 4. Best-fit `const × tbabs (diskbb + compps)` parameters obtained from the XRT + JEM-X + ISGRI spectral analysis

Obs No	C_{JEM-X}	C_{ISGRI}	T_{disk}/T_{seed} (keV)	τ	kT_e (keV)	$\chi^2(\nu)$
(1)	(2)	(3)	(4)	(5)	(6)	(7)
1	0.75 ± 0.05	0.92 ± 0.01	0.204 ± 0.004	$2.20^{+0.20}_{-0.30}$	67 ± 8	1.33 (553)
2	0.78 ± 0.02	0.84 ± 0.04	0.202 ± 0.008	$2.87^{+0.13}_{-0.25}$	57 ± 4	1.44 (447)
3	0.72 ± 0.02	0.91 ± 0.05	0.187 ± 0.008	$1.88^{+0.50}_{-0.17}$	78 ± 8	1.77 (589)
4	0.90 ± 0.03	1.06 ± 0.06	0.177 ± 0.007	$2.42^{+0.43}_{-0.37}$	67 ± 10	1.03 (572)
5	0.73 ± 0.03	0.80 ± 0.06	0.100	$3.00_{-0.37}$	65 ± 5	1.10 (331)

Column (1): Observation number. Column (2-3): Energy independent cross-instrument normalization factors for the JEM-X and ISGRI, . C_{XRT} was frozen at 1. Column (4): disc inner temperature in units of keV. Column (5): Optical depth. Column (6): Electron temperature in units of keV. Column (7): Reduced χ^2 for ν degree of freedom.

Table 5. Best-fit `const × tbabs (diskbb + eqpair)` parameters obtained from the XRT + JEM-X + ISGRI spectral analysis

Obs No	C_{JEM-X}	C_{ISGRI}	T_{disk}/T_{seed} (keV)	l_h/l_s	l_{nth}/l_h	τ_p	$\chi^2(\nu)$
(1)	(2)	(3)	(4)	(5)	(6)	(7)	(8)
			Thermal Comptonization				
1	0.74 ± 0.02	0.94 ± 0.04	0.202 ± 0.004	$7.7^{+0.1}_{-0.4}$	0	$1.46^{+0.07}_{-0.07}$	1.30 (553)
2	0.78 ± 0.02	0.89 ± 0.04	0.198 ± 0.007	$9.3^{+0.3}_{-0.3}$	0	$1.67^{+0.04}_{-0.04}$	1.42 (447)
3	0.71 ± 0.02	1.00 ± 0.04	0.178 ± 0.005	$7.8^{+0.4}_{-0.3}$	0	$1.14^{+0.05}_{-0.04}$	1.69 (589)
4	0.89 ± 0.03	1.05 ± 0.05	0.175 ± 0.010	$10.6^{+0.6}_{-0.7}$	0	$1.68^{+0.10}_{-0.13}$	1.02 (572)
5	0.72 ± 0.03	0.76 ± 0.07	0.100	$20.1^{+1.9}_{-0.8}$	0	$2.54^{+0.34}_{-0.19}$	1.09 (331)
			Hybrid Comptonization				
1	0.78 ± 0.02	0.99 ± 0.05	0.190 ± 0.005	$8.4^{+0.9}_{-0.5}$	$1.00_{-0.09}$	$1.53^{+0.14}_{-0.12}$	1.21 (552)
2	0.81 ± 0.02	0.88 ± 0.03	0.185 ± 0.008	$10.8^{+0.7}_{-0.3}$	$1.00_{-0.26}$	$1.91^{+0.13}_{-0.02}$	1.34 (446)
3	0.75 ± 0.02	1.04 ± 0.04	0.150 ± 0.004	$8.5^{+0.5}_{-0.2}$	$1.00_{-0.02}$	$1.18^{+0.07}_{-0.06}$	1.48 (588)
4	0.92 ± 0.03	1.02 ± 0.05	0.164 ± 0.008	$12.4^{+1.0}_{-0.9}$	$1.00_{-0.40}$	$1.85^{+0.20}_{-0.17}$	1.00 (571)
5	0.72 ± 0.03	0.75 ± 0.07	0.100	$20.9^{+1.3}_{-1.1}$	0.12 ± 0.03	$2.50^{+0.50}_{-0.35}$	1.09 (330)

Column (1): Observation number. Column (2-3): Energy independent cross-instrument normalization factors for the JEM-X, and ISGRI, . C_{XRT} was frozen at 1. Column (4): disc inner temperature in units of keV. Column (5): Ratio of hard to soft compactnesses. Column (6): Ratio of the power supplied to energetic particles which goes into accelerating non-thermal particles. Column (7): Thomson scattering depth. Column (8): Reduced χ^2 for ν degree of freedom.

After the transition, the power-law ratio (PLR, the ratio of the power-law flux to the total flux in the $0.5-10$ keV band) increased to a value of 0.91 within seven days and a rebrightening occurs in all UOIR band on $\sim$ MJD 58397.5. As seen from the changes in the photon index, the spectrum gradually hardens and then starts softening after MJD 58402 while the X-ray flux continues decreasing. During the mini-outburst (starting at MJD 58555) UV and X-ray fluxes were correlated and the system remained in the hard state as indicated by the X-ray spectral power indices.
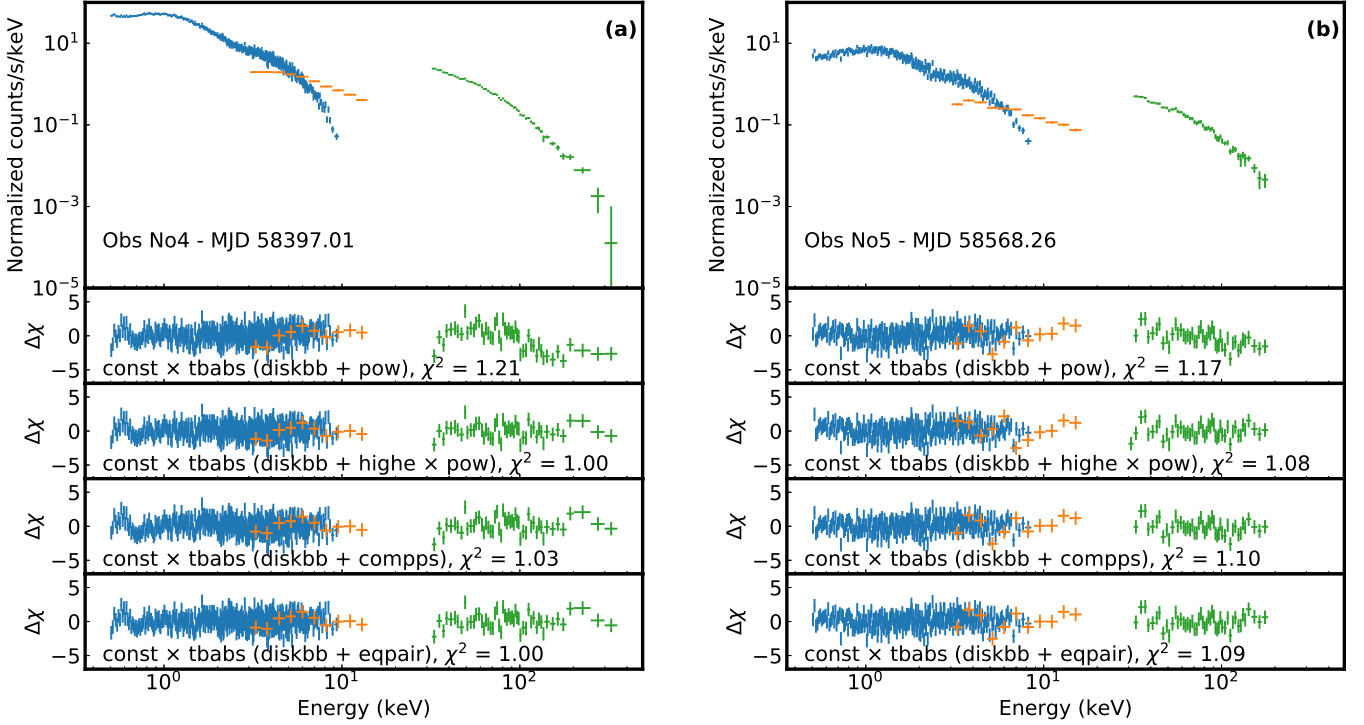
Figure 4: Two broadband spectra compiled from quasi-simultaneous *Swift*/XRT (blue), *INTEGRAL* JEM-X (orange) and ISGRI (green) observations, along with $\Delta\chi$ = (Model - Data) / Error values for various models: (a) Onset of UOIR rebrightening, (b) mini-outburst.

4.2.2 X-ray/γ-ray Spectra

As noted in Section 3.2, we have obtained five X-ray/γ-ray broadband spectra by combining simultaneous *Swift* and *INTEGRAL* observations. The first four spectra were taken in the hard state of the main outburst decay, corresponding to the before/onset of the UOIR rebrightening and the last one on top of the hard mini-outburst (Figure 2). We performed fits in the soft and hard X-ray bands with three models starting with a phenomenological model for comparison with past work. The models get progressively complex with a thermal Comptonization model `compps` (Poutanen & Svensson 1996) and a hybrid Comptonization model `eqpair` (Coppi 1999). We have chosen these models for three reasons: 1. to be able to infer physical characteristics of the Compton scattering in the medium, 2. to search for additional power-law components that may arise from a compact jet, and 3. to make a comparison with past work which uses the same models.

The composite `diskbb + power law` model provided acceptable fits but over-estimated the counts above 100 keV in all spectra. Adding a high-energy cut off (`highecut`) to the model was significantly preferred in the F-test ($P < 10^{-12}$). The folding energies were typically above 100 keV (within 1.6σ error). We calculated 0.5-350 keV fluxes of the source using the best-fit models. The results of the spectral analysis are tabulated in Table 3.

For the `compps` model (Poutanen & Svensson 1996) we used an external `diskbb` component in the analysis of the first four data as justified in Section 4.2.1. We chose a spherical geometry for the corona, assuming the seed photons to be the soft photons originating from the inner edge of the multicolor disc blackbody, and left the electron temperature and the optical depth free but fixed the rest of the model parameters at their default values. We considered both

the thermal and the hybrid plasma cases. For the former, the best-fit parameters as well as the fit statistics are listed in Table 4. Compton reflection was ignored in all fits as it never exceeded 0.05 (3σ upper limit). For the latter, the non-thermal electrons were injected with a power-law of $\Gamma_p = 2.5$ between Lorentz factors $\gamma_{min} = 1.3$ and $\gamma_{max} = 1000$. This resulted in electron temperature pegging at its lowest allowed value of 20 keV and the optical depth pegging at its maximum allowed value of 3. Furthermore, leaving the Γ_p free did not improve the results. We, therefore, conclude that our hybrid plasma fits with the `compps` model was inadequate to explain the data as some parameters are not physically constrained.

For the `eqpair` model we again used an external `diskbb` component in the analysis of the first four data sets. We started with the purely thermal Comptonization case by fixing the l_{nt}/l_h=0. We assumed the seed photon temperature to be that in `diskpn` model, fixed the soft-photon compactness to $l_s = 1$, and the reflection strength R = 0. We left the seed photon temperature T_{seed}, the hard-to-soft compactness l_h/l_s, the optical depth (τ) free but the rest of the parameters fixed at their default values. We also performed fits for the hybrid thermal/non-thermal Comptonization cases by setting the parameters of the electron distribution as in the hybrid `compps` fits and leaving the l_{nt}/l_h parameter free. The results for both the thermal and hybrid Comptonization fits are listed in Table 5. We also show two representative broadband spectra of MAXI J1820+070 together with the $\Delta\chi$ values of all the fit models in Figure 4.

4.2.3 Broadband SEDs

We constructed broadband SEDs for three epochs from the main outburst decay and one from the one from the mini-outburst. The *Swift*/UVOT data were transformed to the flux units during the

photometric extraction (see Section 3.1), and the SMARTS optical/NIR and the TUG optical data were done with the zero points in Bessell et al. (1998). All the UOIR data were dereddened using a color excess of E(B-V) = 0.16 ± 0.05 (see Section 4.2) transformed to wavelength dependent extinction values with the reddening curve in Fitzpatrick & Massa (2007) assuming R_V = 3.1. The errors on the flux densities include uncertainties on both the photometry and the extinction correction.

In order to investigate the spectral components contributing to these bands we performed SED fittings. The best-fit results are shown in Figure 5. The first two SEDs, which were taken before the rebrightening in UOIR band (on MJD 58383.2 and 58393.2,), were in good agreement with the irradiation model diskir (Gierliński et al. 2008, 2009). On the other hand, the SEDs during the rebrightening (MJD 58406.7) and the mini-outburst (MJD 58567.2), produced strong residuals in the NIR-UV region. To improve these last two fits, we added a power-law of Γ=1.6 with a sharp high-energy cut off at 4 × 10^{15} Hz to the model, and obtained acceptable results. The photon index we used here corresponds to spectral index of α = -0.6, a value that is provided by the standard particle acceleration theory (Bednarz & Ostrowski 1998; Kirk et al. 2000). Note that a similar approach was also taken by Shidatsu et al. (2018) to explain the SED during the hard state rise (around MJD 58201).

5 DISCUSSION

5.1 Multiwavelength evolution

Our results show that MAXI J1820+070 exhibited first an increase in the hard X-rays as a signature of the soft-to-intermediate state transition and then a rebrightening concurrently in all of the UOIR band in the hard state. The rebrightening in UOIR band was observed ~ 7 days after the hard state transition. This multiwavelength behaviour is frequently observed in other GBHTs (Kalemci et al. 2005, 2013; Dinçer et al. 2012; Baglio et al. 2018a).

In GBHTs, the origin of the UOIR emission depends on the X-ray state of the source. In the soft and intermediate states, the observed emission is produced by the irradiated outer accretion disc (Russell et al. 2006; Rykoff et al. 2007; Gierliński et al. 2009) whereas in the hard state, starting from the onset of the rebrightening, at least one additional component contributes to the emission in these bands. This is also true for MAXI J1820+070 as its SEDs until the onset of the rebrightening (Figure 5(a) and (b)) are consistent with the irradiated outer accretion disc, while both the one on the top of the rebrightening and the hard mini-outburst (Figure 5(c) and (d)) are only able to provide good fits with an additional power-law component extending from the radio to the UV band (see Section 4.2.3). We looked into this additional power-law component in more detail with the contemporaneous MeerKAT/VLA/SMARTS/UVOT data around MJD 58406.7. In Fig. 5 (c) we showed an overall fit to the SED with a model consistent with other observations in the same figure that we do not have the radio data for. However, when the available radio data are included, as shown in Fig. 6, more details emerge. The radio spectrum is slightly inverted, and a single power-law fit to joint MeerKAT/VLA/SMARTS/UVOT data yields a spectral index α=0.14. While the single power-law connects radio to UOIR data as seen in Fig. 6 with the black dashed lines, the χ^2 is 149.5 for 10 degrees of freedom. The poor fit is a result of the small errors in the radio and infrared flux measurements. We note that since the data are not exactly simultaneous, and both the infrared and radio emissions are variable (see Figs. 2 and 3), the systematic errors are

possibly much larger than the measurement errors. The blue dashed lines show the extended power-law emission with α=0.42 based on the VLA data only (see Shaw et al. 2021, for radio spectral indices based on VLA observations). The infrared to UV frequency band is at the intersection of several emission components operating at the same time, including possibly more than one jet related component (e.g. Rodi et al. 2021), and groups with realistic jet models are welcome to a more complex fit to this data set with the data becoming available. While it may not be exactly clear where the spectral break occurs, adding the radio data strengthens the argument for the presence of a jet related power-law component in this region.

For the hard state observation during the rise of the outburst on March 24, 2018, Shidatsu et al. (2018) claimed that a similar additional power-law component had a jet origin. Zdziarski et al. (2022) and Tetarenko et al. (2021) were both able to show that the broadband SED in the outburst rise with the radio data can be fitted with a jet model. Tetarenko et al. (2021) also used multiwavelength timing studies to deduce additional jet parameters. While the usual interpretation for such a component extending to the near infrared and beyond is the synchrotron emission from jets (Buxton & Bailyn 2004; Kalemci et al. 2005; Russell et al. 2013, and references therein), synchrotron emission from a hot accretion flow is also suggested (Veledina et al. 2013, and references therein). An optical polarimetry study of this source also proved to be inconclusive to distinguish the origin of this additional component (Veledina et al. 2019); however SED fitting with realistic jet models or hot accretion flow model could provide further information.

Bright et al. (2018) detected radio emission from the source with a flux density of ~0.9 mJy at 15.5 GHz on MJD 58385.6 with AMI-LA, ~ 12 days prior to the rebrightening. This is consistent with the jet revival in other sources during their soft-to-hard state transition (Miller-Jones et al. 2012; Corbel et al. 2013; Kalemci et al. 2013; Russell et al. 2013, 2014). Moreover, the radio brightness measured by MeerKAT increased between MJD 58389 and MJD 58397, while the source was fading in all other wavelengths, consistent with a decay rate of 21 days (Bright et al. 2020). For simultaneous and contemporaneous MeerKAT and VLA data, the radio spectrum is inverted, indicating a compact jet. A comparison with the behaviour of GX 339-4 during its 2010-2011 decay can be made here. For GX 339-4, the radio brightening has started around 10 days before the onset of the NIR rebrightening and the first detection of the compact jet. The radio observations before the NIR rebrightening indicated an optically thin emission and became optically thick as the NIR flux increased. The radio flux stayed almost at constant levels for around 10 more days, until the peak of the NIR emission. Afterwards, both NIR and radio fluxes decreased. This has been interpreted as the NIR emission is mostly coming from the compact radio jet during the rebrightening, and the radio spectral index evolves from an optically thin to optically thick emission at the onset of the NIR rebrightening (Corbel et al. 2013). For MAXI J1820+070, the radio flux increases before the UOIR brightening in similar timescales to those of GX 339-4 (though there is no radio spectral index information before MJD 58398). But the striking difference with the behaviour of GX 339-4 is that the radio flux in MAXI J1820+070 is already decreasing between MJD 58398 and MJD 58402, while the optical and UV fluxes are still increasing. Similar behaviour is also observed in MAXI J1836−194 (Russell et al. 2013, 2014) for which the radio emission is already fading with the X-rays, while the optical-IR flux is still rising. While the relative timing of radio flux and the UOIR flux increase is consistent with the standard jet formation model as the jet reestablishes itself brightening first at longer wavelengths be-
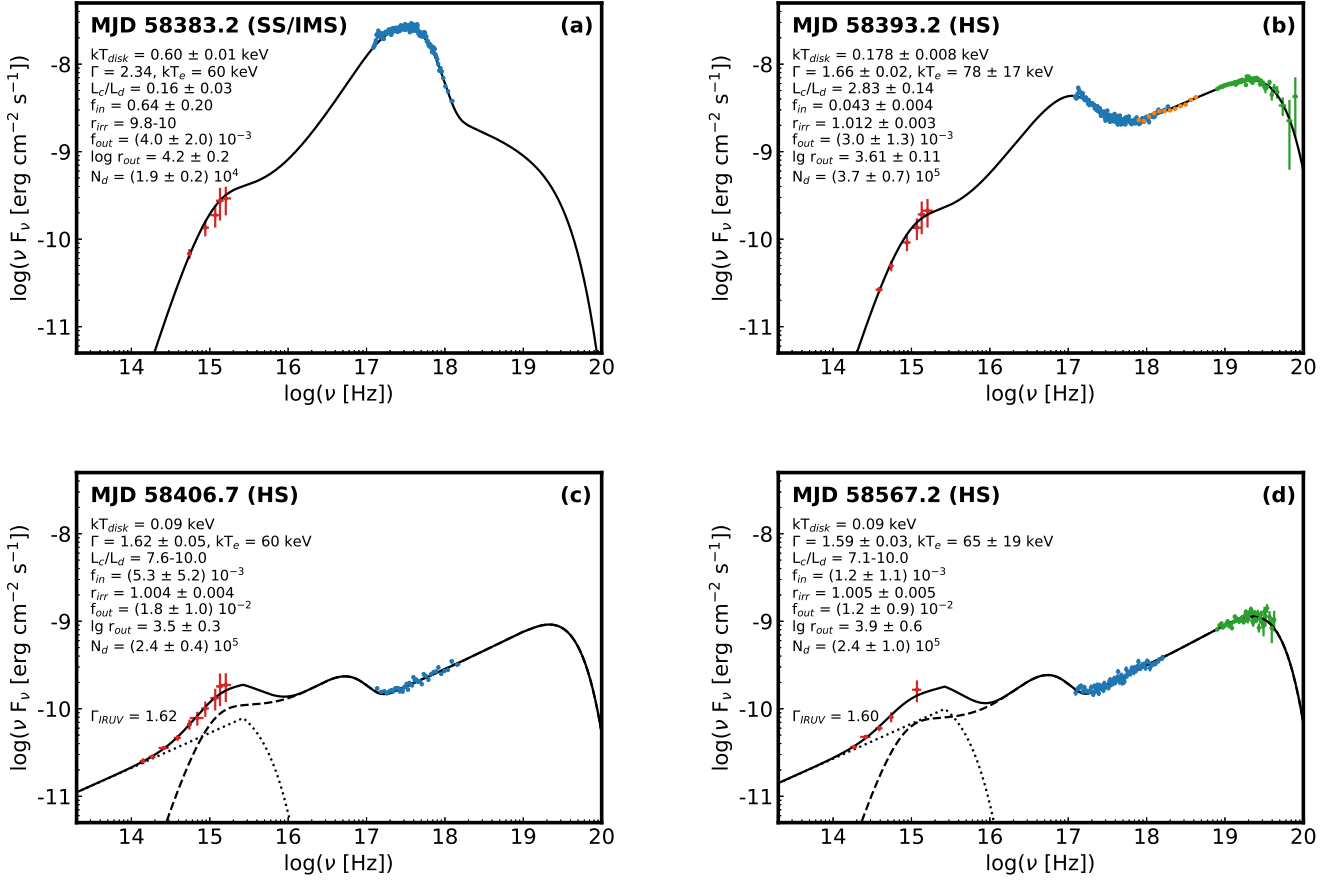
Figure 5: Unfolded broadband SEDs of MAXI J1820+070 from (a) the soft/intermediate state, (b)-(c) the hard states of the main outburst decay, and (c) the hard mini-outburst. The red data points correspond to the UOIR observations from UVOT, TUG and SMARTS. XRT, JEM-X and ISGRI observations are given in blue, orange and green data points, . The SEDs in panel (a)-(b) were fit with the `diskir` model whereas the ones in panel (c)-(d) with the `diskir + power law` composite model (see Section 4.2.3)
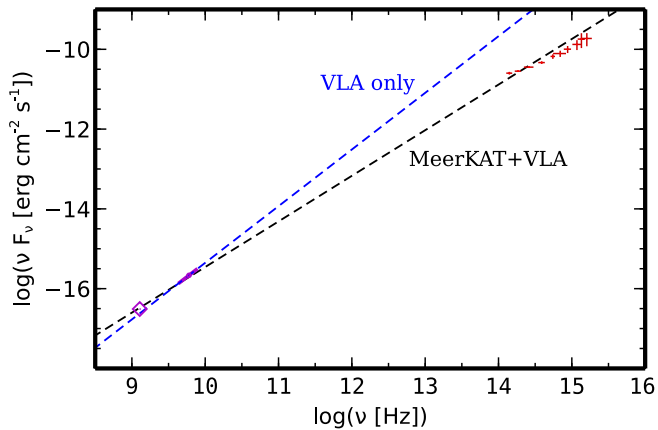.

Figure 6: Unfolded radio-UOIR SED for MAXI J1820+070. MeerKAT (MJD 58405.67) is shown with a diamond, VLA (MJD 58405.90) is shown with a solid line (magenta) between 4.5 - 7.5 GHz with the measured radio spectral index, and the red points are the SMARTS and UVOT fluxes also shown in Fig. 5 (c). The blue dashed line is a power-law with the VLA spectral index, and the black dashed line is obtained by fitting a power-law to the entire data set.

fore UOIR (Miller et al. 2012; Corbel et al. 2013), the subsequent relative evolution changes from source to source.

5.2 High energy behaviour

The high energy behavior can be discussed in terms of the phenomenological and Comptonization model fits to the XRT+JEM-X+ISGRI joint data (see §4.2.2 for all the fit results). For the phenomenological model, the first four observations during the outburst decay provided typical hard state folding energies as given in Table 3. In the model we used, the folding energies are close to the peak energy output of the Comptonization and therefore corresponds to $3kT_e$ where k is the Boltzman constant and T_e is the electron thermal temperature. These temperatures are consistent with the Comptonization electron temperatures with the `compps` fits, which stayed between 60 keV and 80 keV as given in Table 4. Figure 3 shows that these four observations between MJD 58393-58398 occurred at a time when the soft X-ray spectral index is hardening towards its minimum value, right before the rebrightening in UOIR, and during the time that the radio flux is increasing. While there is no apparent evolution in the Comptonization parameters (optical depth τ and T_e of the Comptonizing corona) in the `compps` model fits, there is an apparent drop

in the disk temperature. This can also be seen in soft X-ray fits (see Fig. 4 and Table 2).

The `eqpair` model allows changing a variety of Comptonization and geometrical parameters, and we followed the recommendations in Coppi (1999) to restrict the parameters as described in Section 3. In this model, it is hard to determine the Comptonization parameters hard-to-soft compactness l_h/l_s, the Thomson scattering depth τ_p and the reflection parameters independently if the quality of the data is not great. Therefore, we only used the `eqpair` model to assess the possibility of the hybrid electron energy distribution and also to compare with the past results from other sources. Indeed, the `eqpair` fits indicate that a highly non-thermal model is preferred over pure thermal Comptonization for these observations whereas for the last observation, taken during the mini-outburst, a thermal distribution of electron energies is preferred (see Table 5). Moreover, none of the models, phenomenological or Comptonization, has been improved by adding extra power-law component sometimes associated with the jet emission.

The outburst rise of this source from the hard state to the intermediate states beyond the *NuStar* band (> 70 keV) has been studied with *INTEGRAL*, *MAXI*, and *HXMT*. The region of interest to compare with our data would be ±5 days around MJD 58200. During this time the source is evolving from a very hard state to an intermediate state. Both *MAXI* (Shidatsu et al. 2018) and *HXMT* (You et al. 2021) data fits around that time resulted in Comptonization electron temperatures of 40-80 keV, similar to the temperatures we obtained during the decay. We note that the fit models are different, therefore this is not a direct comparison.

The most detailed high energy study of the source has recently been presented in Zdziarski et al. (2021) for 2 epochs in outburst rise with spectra extending to MeV range using data from *NuStar*, ISGRI and SPI on *INTEGRAL* indicating the presence of a hybrid distribution of electron energies in the Comptonization process together with thermal Comptonization. Their approach with two Comptonization model does not necessarily indicate an additional component from a jet. We note that this comparison with the outburst rise could only be done indirectly due to two important reasons. Thanks to the quality of outburst rise data, together with high spectral resolution of *NuSTAR* and the extended energy range to 2 MeV with the INTEGRAL SPI and PiCSIT, Zdziarski et al. (2021) were able to obtain strong constraints on accretion geometry and associated physical parameters. Moreover, they used different Comptonization models (`reflkerr` and `reflkerr.bb`, see Zdziarski et al. 2021 and references therein) more appropriate for the data they use. While the thermal Comptonization part still uses `compps` in the background, the non-thermal part is calculated self-consistently in a different manner than `eqpair`. We should note that although our data also prefers non-thermal distribution of electron energies, the quality of the spectra prohibits us constraining physical parameters any further.

We could also compare our results with the other GBHTs studied with *INTEGRAL* during the outburst decays. With our *INTEGRAL* observing program of GBHTs during the decay we have observed XTE J1752−223 (Chun et al. 2013) and SWIFT J1745−26 (Kalemci et al. 2014). For both of these sources, the *INTEGRAL* observations took place after the source reached its hardest levels. In a sense, the observations of MAXI J1820+070 is complementary to the already present hard state observations, as the current data set includes the evolution of the system towards the hard state. For the simple `highecut` fits done in the same way for all observations during the decay, one can observe that both XTE J1752−223 and SWIFT J1745−26 have higher folding energies compared to MAXI J1820+070. In parallel to this, when fitted with `compps`,

we observe that XTE J1752−223 has a higher temperature in the Comptonizing medium, whereas for SWIFT J1745−26, it either has a higher temperature, or higher optical depth. These results are not surprising at all, for MAXI J1820+070 both the electron temperature and density is lower compared to those of other sources already deep in the hard state. On the other hand, our observations do not allow us to track the evolution of the Comptonization parameters with the given errors, the only significant evolution we can observe is in the decreasing disc flux and the temperature. Interestingly, the `eqpair` fits in SWIFT J1745−26 deep in the hard state does not necessarily require non-thermal electron distribution. For XTE J1752−223, the thermal Comptonization is a good fit as well. The lack of data beyond MJD 58400 makes it hard to discuss if there is an evolution from hybrid to thermal distribution in outburst decays, this is something that can only be tested with observations catching both the transition and hard state observations in one source.

Finally, we can compare behaviour of MAXI J1820+070 during the mini-outburst. All three sources we investigated with *INTEGRAL* during the outburst decay (Kalemci et al. 2014; Chun et al. 2013) and V404 Cyg showed such late brightening events after the main outburst (Kajava et al. 2018). For XTE J1752−223, SWIFT J1745−26, and MAXI J1820+070, the episodes started ~60, ~100, and ~165 days after the soft-to-hard state transition in the main outburst decay, respectively. In all three cases, the increase in the hard and the soft X-ray flux is accompanied with an increase in OIR band and lasted for around 40 days. Both SWIFT J1745−26 and MAXI J1820+070 spectral fits indicated that thermal Comptonization is enough to explain the hard X-ray spectra. Similarly, the June 2015 mini-outburst of V404 Cyg occurred ~150 days after the main outburst, and showed X-ray and radio flares, and rich P-Cygni profiles indicative of winds in the hard state (Muñoz-Darias et al. 2017). The spectral analysis indicated hard state with behavior similar to the beginning of the regular outburst (Kajava et al. 2018).

For MAXI J1820+070, the apparent lack of any delay between UOIR emission and hard X-rays (which is also observed in XTE J1752−223 Chun et al. 2013) and spectral indices starting from the hard levels compared to the softer low flux observations (Shaw et al. 2021), all indicate that the mini-outburst behaves like a start of a new outburst consistent with additional mass accretion on to the compact object perhaps due to the change of the nature of emission during the state transition to the hard state. However, for the four cases investigated with INTEGRAL, the mini-outbursts did not make a transition to the soft state. This is the case for most sources, but for MAXI J1535−571, the multiple outbursts seemed to go into softer states as indicated through their HIDs (Cúneo et al. 2020). We note that MAXI J1535−571 mini-outbursts, while separated by days, became quite bright, and the source never entered the quiescence. The origin and behavior of the increased flux levels after the main outburst decays could be different from source to source showing the importance of following the entire outburst with multiwavelength coverage.

6 SUMMARY

In this work, we have studied the spectral properties of MAXI J1820+070 during the decay of the 2018 outburst and the subsequent mini-outburst in March 2019. Using quasi-simultaneous data from INTEGRAL, Swift, SMARTS and TUG telescopes, we have investigated the evolution of spectral parameters from a multiwavelength perspective to understand the physical mechanisms governing

the increase in flux levels detected at the final stage of the outburst. The main findings from our analysis can be summarised as follows:

(i) The source underwent a rebrightening event in hard X-rays and the UOIR band between MJD 58380-58440, close to the end of the main outburst. A few days after the radio detection, it transitioned from the intermediate-to-hard state on MJD 58390. The rebrightening started in the hard X-rays first and was followed by the UOIR bands. We have found the onset of the rebrightening in the V-band on MJD 58397.5, a week after the hard state transition, a well-known multiwavelength behaviour seen in other GBHTs observed at the outburst decay.

(ii) We showed that the source stayed in the hard state during its ~40-day long mini-outburst. In contrast to the rebrightening, it started 165-days after the soft-to-hard state transition at the main outburst decay and showed a similar trend in its multiwavelength light curves. We compared the spectral properties and the measured time scales of mini-outburst with other GBHTs investigated with INTEGRAL and concluded that it behaved like a new outburst.

(iii) We have performed broadband spectral fitting on the joint XRT+JEM-X+ISGRI data using phenomenological and Comptonization models. A non-thermal electron energy distribution is preferred over a pure thermal distribution for the rebrightening phase, however, the mini-outburst case can be fitted with a pure thermal Comptonization model. Furthermore, none of the models has been improved by adding an extra power-law component (possibly related to the jet) in X-rays in contrast to models presented in the outburst rise. We stress that the quality of the data in the outburst rise is significantly better than that of outburst decay.

(iv) The SEDs until the onset of the rebrightening are consistent with the irradiated outer accretion disc, while the ones close to the UOIR and mini-outburst peaks provide good fits only with an additional power-law component in the NIR-UV band. We looked into the detail of this power-law component for the data around MJD 58406.7 by adding the radio observations to the fits and discussed that it might have a jet origin though we could not constrain the exact location of the spectral break.

DATA AVAILABILITY

The *Swift* data underlying this article are publicly available in the HEASARC Data Archieve at https://heasarc.gsfc.nasa.gov/. The *INTEGRAL* data with ObsIDs 15400050001 (PI: E. Kalemci) and 16700020001 can be reached at https://www.isdc.unige.ch/integral/archive. The MAXI/GSC data used in Fig. 2 can be downloaded from http://maxi.riken.jp/star_data/J1820+071/J1820+071.html. The SMARTS data (PI: C. Bailyn) are available from https://astroarchive.noao.edu/. The TUG data (PI: T. Dinçer) will be shared on reasonable request to the corresponding author. All the generated data underlying this study are available in the article and in its online supplementary material.

REFERENCES

Adachi R., et al., 2020, The Astronomer's Telegram, 13502, 1
Arnaud K. A., 1996, in Jacoby G. H., Barnes J., eds, Astronomical Society of the Pacific Conference Series Vol. 101, Astronomical Data Analysis Software and Systems V. p. 17
Atri P., et al., 2020, MNRAS, 493, L81
Augusteijn T., Kuulkers E., Shaham J., 1993, A&A, 279, L13
Baglio M. C., et al., 2018a, ApJ, 867, 114
Baglio M. C., Russell D., Qaissieh T. A., Palado A., Gabuya A., Shivkumar H., Lewis F., 2018b, The Astronomer's Telegram, 12128
Baglio M. C., Russell D. M., Saikia P., Bramich D. M., Lewis F., 2021, The Astronomer's Telegram, 14492, 1
Bahramian A., Motta S., Atri P., Miller-Jones J., 2019, The Astronomer's Telegram, 12573, 1
Barthelmy S. D., et al., 2005, Space Sci. Rev., 120, 143
Bednarz J., Ostrowski M., 1998, Physical Review Letters, 80, 3911
Belloni T. M., 2010, in Belloni T., ed., Lecture Notes in Physics, Berlin Springer Verlag Vol. 794, Lecture Notes in Physics, Berlin Springer Verlag. p. 53 (arXiv:0909.2474), doi:10.1007/978-3-540-76937-8_3
Belloni T. M., Motta S. E., 2016, in Bambi C., ed., Astrophysics and Space Science Library Vol. 440, Astrophysics of Black Holes: From Fundamental Aspects to Latest Developments. p. 61 (arXiv:1603.07872), doi:10.1007/978-3-662-52859-4_2
Belloni T., Homan J., Casella P., van der Klis M., Nespoli E., Lewin W. H. G., Miller J. M., Méndez M., 2005, A&A, 440, 207
Bessell M. S., Castelli F., Plez B., 1998, A&A, 333, 231
Bright J., Motta S., Fender R., 2018, The Astronomer's Telegram, 12061
Bright J., Motta S., Williams D., Fender R., Woudt P., Miller-Jones J., 2019, The Astronomer's Telegram, 13041, 1
Bright J. S., et al., 2020, Nature Astronomy, 4, 697
Burrows D. N., et al., 2005, Space Sci. Rev., 120, 165
Buxton M. M., Bailyn C. D., 2004, ApJ, 615, 880
Buxton M. M., Bailyn C. D., Capelo H. L., Chatterjee R., Dinçer T., Kalemci E., Tomsick J. A., 2012, AJ, 143, 130
Cangemi F., et al., 2021, arXiv e-prints, p. arXiv:2102.04773
Carotenuto F., et al., 2021, MNRAS, 504, 444
Chen W., Shrader C. R., Livio M., 1997, ApJ, 491, 312
Chun Y. Y., et al., 2013, ApJ, 770, 10
Coppi P. S., 1999, in Poutanen J., Svensson R., eds, Astronomical Society of the Pacific Conference Series Vol. 161, High Energy Processes in Accreting Black Holes. p. 375 (arXiv:astro-ph/9903158)
Corbel S., Fender R. P., Tzioumis A. K., Nowak M., McIntyre V., Durouchoux P., Sood R., 2000, A&A, 359, 251
Corbel S., et al., 2013, MNRAS, 431, L107
Coriat M., Corbel S., Buxton M. M., Bailyn C. D., Tomsick J. A., Körding E., Kalemci E., 2009, MNRAS, 400, 123
Coriat M., Fender R. P., Dubus G., 2012, MNRAS, 424, 1991
Corral-Santana J. M., Casares J., Muñoz-Darias T., Bauer F. E., Martínez-Pais I. G., Russell D. M., 2016, A&A, 587, A61
Courvoisier T. J.-L., et al., 2003, A&A, 411, L53
Cúneo V. A., et al., 2020, MNRAS, 496, 1001
DePoy D. L., et al., 2003, in Iye M., Moorwood A. F. M., eds, Proc. SPIE Vol. 4841, Instrument Design and Performance for Optical/Infrared Ground-based Telescopes. pp 827–838, doi:10.1117/12.459907

Denisenko D., 2018, The Astronomer's Telegram, 11400, 1
Dinçer T., Kalemci E., Buxton M. M., Bailyn C. D., Tomsick J. A., Corbel S., 2012, ApJ, 753, 55
Dinçer T., Kalemci E., Tomsick J. A., Buxton M. M., Bailyn C. D., 2014, ApJ, 795, 74
Dunn R. J. H., Fender R. P., Körding E. G., Belloni T., Cabanac C., 2010, MNRAS, 403, 61
Ertan Ü., Alpar M. A., 2002, A&A, 393, 205
Esin A. A., McClintock J. E., Narayan R., 1997, ApJ, 489, 865
Espinasse M., et al., 2020, ApJ, 895, L31
Fender R. P., 2001, MNRAS, 322, 31
Fender R., Gallo E., 2014, Space Sci. Rev., 183, 323
Fender R., et al., 1999, ApJ, 519, L165
Fender R. P., Hjellming R. M., Tilanus R. P. J., Pooley G. G., Deane J. R., Ogley R. N., Spencer R. E., 2001, MNRAS, 322, L23
Fender R. P., Homan J., Belloni T. M., 2009, MNRAS, 396, 1370
Fitzpatrick E. L., Massa D., 2007, ApJ, 663, 320
Gallo E., Fender R. P., Pooley G. G., 2003, MNRAS, 344, 60
Gehrels N., et al., 2004, ApJ, 611, 1005
Gendreau K. C., et al., 2016, in den Herder J.-W. A., Takahashi T., Bautz M., eds, Society of Photo-Optical Instrumentation Engineers (SPIE) Conference Series Vol. 9905, Space Telescopes and Instrumentation 2016: Ultraviolet to Gamma Ray. p. 99051H, doi:10.1117/12.2231304
Gierliński M., Done C., Page K., 2008, MNRAS, 388, 753
Gierliński M., Done C., Page K., 2009, MNRAS, 392, 1106
Gilfanov M., 2010, in Belloni T., ed., Lecture Notes in Physics, Berlin Springer Verlag Vol. 794, Lecture Notes in Physics, Berlin Springer Verlag. p. 17 (arXiv:0909.2567), doi:10.1007/978-3-540-76937-8_2
Hankins M., et al., 2019, The Astronomer's Telegram, 13044, 1
Homan J., Wijnands R., van der Klis M., Belloni T., van Paradijs J., Klein-Wolt M., Fender R., Méndez M., 2001, ApJS, 132, 377
Homan J., Buxton M., Markoff S., Bailyn C. D., Nespoli E., Belloni T., 2005, ApJ, 624, 295
Homan J., et al., 2018, The Astronomer's Telegram, 12068
Homan J., et al., 2020, ApJ, 891, L29
Homan J., et al., 2021, The Astronomer's Telegram, 14495, 1
Kajava J. J. E., Motta S. E., Sánchez-Fernández C., Kuulkers E., 2018, A&A, 616, A129
Kalemci E., Tomsick J. A., Buxton M. M., Rothschild R. E., Pottschmidt K., Corbel S., Brocksopp C., Kaaret P., 2005, ApJ, 622, 508
Kalemci E., Dinçer T., Tomsick J. A., Buxton M. M., Bailyn C. D., Chun Y. Y., 2013, ApJ, 779, 95
Kalemci E., et al., 2014, MNRAS, 445, 1288
Kawamuro T., et al., 2018, The Astronomer's Telegram, 11399
Kirk J. G., Guthmann A. W., Gallant Y. A., Achterberg A., 2000, ApJ, 542, 235
Krimm H. A., et al., 2013, ApJS, 209, 14
Landolt A. U., 1992, AJ, 104, 340
Lebrun F., et al., 2003, A&A, 411, L141
Lund N., et al., 2003, A&A, 411, L231
Maccarone T. J., 2003, A&A, 409, 697
Markoff S., Falcke H., Fender R., 2001, A&A, 372, L25
Markoff S., Nowak M., Corbel S., Fender R., Falcke H., 2003, A&A, 397, 645
Markoff S., Nowak M. A., Wilms J., 2005, ApJ, 635, 1203
Matsuoka M., et al., 2009, PASJ, 61, 999
McClintock J. E., Remillard R. A., 2006, Black hole binaries. Cambridge University Press, pp 157–213
Meyer F., Meyer-Hofmeister E., 1981, A&A, 104, L10
Miller-Jones J. C. A., et al., 2012, MNRAS, 421, 468
Miller J. M., Homan J., Steeghs D., Rupen M., Hunstead R. W., Wijnands R., Charles P. A., Fabian A. C., 2006, ApJ, 653, 525
Miller J. M., Pooley G. G., Fabian A. C., Nowak M. A., Reis R. C., Cackett E. M., Pottschmidt K., Wilms J., 2012, ApJ, 757, 11
Mitsuda K., et al., 1984, PASJ, 36, 741
Muñoz-Darias T., et al., 2017, MNRAS, 465, L124
Poutanen J., 1998, in Abramowicz M. A., Björnsson G., Pringle J. E., eds, Theory of Black Hole Accretion Disks. pp 100–122 (arXiv:astro-ph/9805025)
Poutanen J., Svensson R., 1996, ApJ, 470, 249

Poutanen J., Krolik J. H., Ryde F., 1997, MNRAS, 292, L21
Remillard R. A., McClintock J. E., 2006, ARA&A, 44, 49
Reynolds M. T., Miller J. M., 2013, ApJ, 769, 16
Rodi J., Tramacere A., Onori F., Bruni G., Sànchez-Fernàndez C., Fiocchi M., Natalucci L., Ubertini P., 2021, ApJ, 910, 21
Roming P. W. A., et al., 2005, Space Sci. Rev., 120, 95
Roques J.-P., Jourdain E., 2019, ApJ, 870, 92
Russell D. M., Fender R. P., Hynes R. I., Brocksopp C., Homan J., Jonker P. G., Buxton M. M., 2006, MNRAS, 371, 1334
Russell D. M., Maitra D., Dunn R. J. H., Markoff S., 2010, MNRAS, 405, 1759
Russell D. M., et al., 2012, MNRAS, 419, 1740
Russell D. M., et al., 2013, MNRAS, 429, 815
Russell T. D., Soria R., Miller-Jones J. C. A., Curran P. A., Markoff S., Russell D. M., Sivakoff G. R., 2014, MNRAS, 439, 1390
Russell T. D., et al., 2019a, ApJ, 883, 198
Russell D. M., Baglio M. C., Lewis F., 2019b, The Astronomer's Telegram, 12534, 1
Rykoff E. S., Miller J. M., Steeghs D., Torres M. A. P., 2007, ApJ, 666, 1129
Sai H., et al., 2021, MNRAS, 504, 4226
Sasaki R., et al., 2020, The Astronomer's Telegram, 13530, 1
Schlafly E. F., Finkbeiner D. P., 2011, ApJ, 737, 103
Shakura N. I., Sunyaev R. A., 1973, A&A, 24, 337
Shaw A. W., et al., 2021, ApJ, 907, 34
Shidatsu M., et al., 2018, ApJ, 868, 54
Shidatsu M., Nakahira S., Murata K. L., Adachi R., Kawai N., Ueda Y., Negoro H., 2019, ApJ, 874, 183
Skrutskie M. F., et al., 2006, AJ, 131, 1163
Stetson P. B., 1987, PASP, 99, 191
Subasavage J. P., Bailyn C. D., Smith R. C., Henry T. J., Walter F. M., Buxton M. M., 2010, in Observatory Operations: Strategies, Processes, and Systems III. p. 77371C, doi:10.1117/12.859145
Sunyaev R. A., Truemper J., 1979, Nature, 279, 506
Tanaka Y., Lewin W. H. G., 1995, in X-ray Binaries. pp 126–174
Tanaka Y., Shibazaki N., 1996, ARA&A, 34, 607
Tetarenko A. J., et al., 2015, ApJ, 805, 30
Tetarenko B. E., Sivakoff G. R., Heinke C. O., Gladstone J. C., 2016, ApJS, 222, 15
Tetarenko A. J., et al., 2021, MNRAS, 504, 3862
Tody D., 1986, in Crawford D. L., ed., Proc. SPIE Vol. 627, Instrumentation in astronomy VI. p. 733, doi:10.1117/12.968154
Tody D., 1993, in Hanisch R. J., Brissenden R. J. V., Barnes J., eds, Astronomical Society of the Pacific Conference Series Vol. 52, Astronomical Data Analysis Software and Systems II. p. 173
Tomsick J. A., Kalemci E., Corbel S., Kaaret P., 2003, ApJ, 592, 1100
Torres M. A. P., Casares J., Jiménez-Ibarra F., Muñoz-Darias T., Armas Padilla M., Jonker P. G., Heida M., 2019, ApJ, 882, L21
Torres M. A. P., Casares J., Jiménez-Ibarra F., Álvarez-Hernández A., Muñoz-Darias T., Armas Padilla M., Jonker P. G., Heida M., 2020, ApJ, 893, L37
Trushkin S. A., Nizhelskij N. A., Tsybulev P. G., Erkenov A., 2018, The Astronomer's Telegram, 11439, 1
Ulowetz J., Myers G., Patterson J., 2019, The Astronomer's Telegram, 12567, 1
Uttley P., et al., 2018, The Astronomer's Telegram, 11423, 1
Vadawale S. V., Rao A. R., Naik S., Yadav J. S., Ishwara-Chandra C. H., Pramesh Rao A., Pooley G. G., 2003, ApJ, 597, 1023
Vedrenne G., et al., 2003, A&A, 411, L63
Veledina A., Poutanen J., Vurm I., 2013, MNRAS, 430, 3196
Veledina A., et al., 2019, A&A, 623, A75
Verner D. A., Ferland G. J., Korista K. T., Yakovlev D. G., 1996, ApJ, 465, 487
Vozza D., Ali S., Balakrishnan M., Chen J., Kebebe N., Miller J. M., Reynolds M., Tetarenko B. E., 2019, The Astronomer's Telegram, 12688, 1
Wilms J., Allen A., McCray R., 2000, ApJ, 542, 914
Winkler C., et al., 2003, A&A, 411, L1
Wood C. M., et al., 2021, MNRAS, 505, 3393
Xu Y., Harrison F., Tomsick J., 2019, The Astronomer's Telegram, 13025, 1
You B., et al., 2021, Nature Communications, 12, 1025
Zdziarski A. A., Gierliński M., 2004, Progress of Theoretical Physics Supplement, 155, 99

Zdziarski A. A., et al., 2021, arXiv e-prints, p. arXiv:2104.04316
Zdziarski A. A., Tetarenko A. J., Sikora M., 2022, ApJ, 925, 189
Zhang G.-B., et al., 2019, ApJ, 876, 5
Zhu H., Tian W., Li A., Zhang M., 2017, MNRAS, 471, 3494

SUPPORTING INFORMATION

Supplementary data are available at MNRAS online

APPENDIX A: UOIR MONITORING DATA FROM SWIFT/UVOT, TUG AND SMARTS.

This paper has been typeset from a TeX/LaTeX file prepared by the author.

Table A1. *Swift*/UVOT measurements.

Date	*V* mag	Date	*U* mag	Date	*M2* mag	Date	*W1* mag	Date	*W2* mag
383.1560	14.167 ± 0.027	378.9005	12.929 ± 0.024	378.8955	12.790 ± 0.032	378.8986	12.683 ± 0.032	378.9030	12.626 ± 0.032
386.0776	14.074 ± 0.037	383.1625	13.204 ± 0.024	383.1581	13.013 ± 0.033	383.1608	12.945 ± 0.033	383.1534	12.879 ± 0.032
387.6087	14.073 ± 0.027	386.0809	13.070 ± 0.027	386.0786	12.990 ± 0.036	386.0799	12.849 ± 0.036	386.0763	12.819 ± 0.033
388.9240	14.262 ± 0.029	387.6148	13.185 ± 0.025	387.6107	13.095 ± 0.034	387.6132	12.948 ± 0.033	387.6062	12.943 ± 0.032
390.3235	14.374 ± 0.029	388.9300	13.360 ± 0.026	388.9260	13.241 ± 0.034	388.9285	13.152 ± 0.034	388.9215	13.086 ± 0.032
391.4571	14.472 ± 0.030	390.3305	13.444 ± 0.024	390.3258	13.328 ± 0.034	390.3287	13.220 ± 0.034	390.3207	13.158 ± 0.032
392.5861	14.495 ± 0.031	391.4516	13.624 ± 0.026	391.4597	13.411 ± 0.033	391.4499	13.289 ± 0.034	391.4543	13.197 ± 0.032
393.2410	14.517 ± 0.032	392.5808	13.650 ± 0.027	392.5888	13.405 ± 0.033	392.5792	13.326 ± 0.034	392.5834	13.259 ± 0.032
394.7634	14.696 ± 0.061	393.2472	13.627 ± 0.025	393.2430	13.409 ± 0.035	393.2455	13.306 ± 0.034	393.2385	13.238 ± 0.032
395.4312	14.656 ± 0.033	394.7657	13.706 ± 0.030	394.7641	13.458 ± 0.043	394.7650	13.451 ± 0.043	394.7625	13.318 ± 0.037
397.0990	14.649 ± 0.033	395.4377	13.764 ± 0.027	395.4333	13.497 ± 0.035	395.4360	13.465 ± 0.034	395.4285	13.341 ± 0.032
400.0145	14.240 ± 0.037	397.1056	13.754 ± 0.026	397.1012	13.623 ± 0.035	397.1038	13.498 ± 0.035	397.0964	13.414 ± 0.032
402.2814	14.027 ± 0.033	400.0180	13.586 ± 0.047	400.0157	13.489 ± 0.038	400.0173	13.351 ± 0.037	400.0130	13.298 ± 0.034
404.2669	14.016 ± 0.025	402.2851	13.327 ± 0.029	402.2826	13.326 ± 0.037	402.2842	13.133 ± 0.036	402.2798	13.209 ± 0.034
406.7369	14.203 ± 0.029	404.2733	13.367 ± 0.030	404.2691	13.360 ± 0.034	404.2719	13.198 ± 0.034	404.2641	13.262 ± 0.032
408.2500	14.141 ± 0.028	406.7427	13.535 ± 0.029	406.7389	13.476 ± 0.035	406.7413	13.325 ± 0.034	406.7345	13.373 ± 0.033
410.3100	14.276 ± 0.026	408.2563	13.512 ± 0.025	408.2521	13.477 ± 0.035	408.2546	13.281 ± 0.034	408.2475	13.353 ± 0.032
412.0373	14.278 ± 0.023	410.3185	13.505 ± 0.023	410.3127	13.531 ± 0.034	410.3161	13.368 ± 0.033	410.3066	13.393 ± 0.032
417.4849	14.570 ± 0.026	412.1036	13.608 ± 0.026	412.0404	13.562 ± 0.034	412.1023	13.460 ± 0.038	412.0331	13.423 ± 0.032
419.6093	14.507 ± 0.041	417.4949	13.818 ± 0.024	417.4882	13.831 ± 0.034	417.4923	13.673 ± 0.033	417.4808	13.647 ± 0.032
424.6648	14.782 ± 0.030	419.6129	13.972 ± 0.032	419.6105	13.836 ± 0.041	419.6120	13.640 ± 0.039	419.6078	13.731 ± 0.036
425.4588	14.943 ± 0.042	424.6736	14.189 ± 0.073	424.6680	14.061 ± 0.035	424.6719	13.932 ± 0.034	424.6609	13.940 ± 0.033
426.6530	14.793 ± 0.032	425.4641	14.126 ± 0.028	425.4605	14.138 ± 0.040	425.4626	13.903 ± 0.038	425.4567	13.998 ± 0.035
428.1772	14.970 ± 0.036	428.1847	14.182 ± 0.026	428.1796	14.200 ± 0.037	428.1827	14.096 ± 0.036	426.6489	13.992 ± 0.032
430.7013	15.165 ± 0.048	430.7065	14.454 ± 0.032	430.7030	14.309 ± 0.041	430.7051	14.207 ± 0.040	428.1741	14.072 ± 0.034
434.3607	15.328 ± 0.040	434.3690	14.474 ± 0.033	434.3636	14.600 ± 0.039	434.3672	14.445 ± 0.037	430.6993	14.275 ± 0.036
436.5399	15.417 ± 0.043	436.5481	14.720 ± 0.033	436.5427	14.782 ± 0.041	436.5462	14.587 ± 0.038	434.3571	14.576 ± 0.035
438.5992	15.704 ± 0.046	438.6096	14.782 ± 0.029	438.6027	15.007 ± 0.040	438.6070	14.630 ± 0.037	436.5365	14.577 ± 0.035
440.1928	15.756 ± 0.047	440.2033	15.125 ± 0.031	440.1963	15.167 ± 0.042	440.2006	14.931 ± 0.039	438.5950	14.899 ± 0.035
559.1445	14.226 ± 0.038	559.1482	13.497 ± 0.028	558.8623	13.541 ± 0.031	555.8067	14.042 ± 0.031	440.1884	14.936 ± 0.035
566.2450	13.876 ± 0.024	564.2554	13.311 ± 0.021	559.1457	13.478 ± 0.039	559.1472	13.273 ± 0.037	557.0690	13.893 ± 0.032
–	–	566.2516	13.310 ± 0.026	562.1250	13.170 ± 0.031	563.1209	12.994 ± 0.031	559.1431	13.384 ± 0.034
–	–	572.1505	13.448 ± 0.021	566.2472	13.197 ± 0.034	566.2500	12.965 ± 0.033	561.8594	13.061 ± 0.031
–	–	576.0631	13.520 ± 0.021	571.0312	13.311 ± 0.032	567.1729	13.096 ± 0.031	565.1816	13.248 ± 0.031
–	–	–	–	574.3344	13.360 ± 0.031	575.1414	13.339 ± 0.031	566.2423	13.096 ± 0.032
–	–	–	–	–	–	–	–	573.3455	13.230 ± 0.031
–	–	–	–	–	–	–	–	577.0589	13.419 ± 0.031

Note: Observation time is given as Date = MJD - 58000 in days.

Table A2. Measurements of optical and NIR data from SMARTS observations. A full version of this table is available online.

Date	*B* mag	Date	*V* mag	Date	*I* mag
406.0396	14.513 ± 0.006	406.0355	14.195 ± 0.004	406.0314	13.508 ± 0.015
406.0406	14.531 ± 0.005	406.0365	14.184 ± 0.005	406.0324	13.489 ± 0.015
406.0416	14.550 ± 0.005	406.0375	14.184 ± 0.004	406.0334	13.502 ± 0.015
406.0426	14.560 ± 0.005	406.0385	14.156 ± 0.004	406.0344	13.519 ± 0.016
407.0118	14.507 ± 0.005	407.0077	14.199 ± 0.004	407.0036	13.548 ± 0.016
⋮	⋮	⋮	⋮	⋮	⋮

	J mag		*H* mag		*K* mag
406.0354	12.724 ± 0.017	406.0313	12.092 ± 0.030	407.0117	11.412 ± 0.080
407.0076	12.760 ± 0.017	407.0035	12.123 ± 0.031	407.9972	11.598 ± 0.080
407.9930	12.810 ± 0.017	407.9889	12.227 ± 0.030	409.0086	11.626 ± 0.080
409.0045	12.807 ± 0.017	409.0004	12.248 ± 0.031	–	–
410.9973	12.901 ± 0.017	410.9932	12.366 ± 0.031	–	–
⋮	⋮	⋮	⋮	–	–

Note: *Date = MJD - 58000 in days

Note: Effective wavelengths (λ_{eff}):

BVI filters, λ_{eff} = 439.2, 578.6 and 817.6 nm,

JHK filters, λ_{eff} = 1.24, 1.62 and 2.13 μm.

Table A3. TUG optical measurements.

Date	*B* mag	Date	*V* mag	Date	*R* mag	Date	*I* mag
397.7037	14.783 ± 0.006	389.7978	14.252 ± 0.004	389.7987	14.205 ± 0.005	389.7994	13.892 ± 0.015
397.7052	14.826 ± 0.006	389.8000	14.239 ± 0.005	389.8009	14.225 ± 0.005	389.8016	13.881 ± 0.015
397.7060	14.838 ± 0.005	389.8022	14.257 ± 0.004	389.8031	14.238 ± 0.006	389.8038	13.864 ± 0.015
397.7088	14.826 ± 0.005	389.8045	14.250 ± 0.004	389.8053	14.232 ± 0.006	389.8060	13.876 ± 0.015
397.7110	14.840 ± 0.004	389.8067	14.253 ± 0.004	389.8075	14.237 ± 0.006	389.8082	13.901 ± 0.016
397.7126	14.840 ± 0.004	389.8089	14.242 ± 0.004	389.8097	14.229 ± 0.011	389.8104	13.859 ± 0.015
398.6950	14.514 ± 0.006	389.8111	14.242 ± 0.005	389.8119	14.232 ± 0.007	389.8126	13.877 ± 0.017
398.6961	14.482 ± 0.006	389.8133	14.260 ± 0.004	389.8141	14.211 ± 0.009	389.8148	13.874 ± 0.016
398.6969	14.501 ± 0.006	389.8155	14.242 ± 0.004	389.8164	14.229 ± 0.007	389.8170	13.886 ± 0.016
–	–	389.8177	14.263 ± 0.004	389.8186	14.220 ± 0.014	389.8192	13.916 ± 0.021
–	–	393.7985	14.457 ± 0.004	393.7994	14.454 ± 0.007	393.8000	14.137 ± 0.017
–	–	393.8007	14.461 ± 0.005	393.8016	14.451 ± 0.006	393.8022	14.148 ± 0.016
–	–	393.8029	14.469 ± 0.004	393.8038	14.465 ± 0.006	393.8044	14.120 ± 0.015
–	–	393.8051	14.463 ± 0.004	393.8060	14.446 ± 0.005	393.8066	14.096 ± 0.016
–	–	393.8073	14.459 ± 0.004	393.8082	14.446 ± 0.005	393.8088	14.120 ± 0.016
–	–	393.8095	14.475 ± 0.004	393.8104	14.468 ± 0.006	393.8111	14.121 ± 0.016
–	–	393.8117	14.476 ± 0.005	393.8126	14.469 ± 0.007	393.8133	14.143 ± 0.016
–	–	393.8139	14.485 ± 0.004	393.8148	14.477 ± 0.007	393.8155	14.130 ± 0.016
–	–	393.8161	14.469 ± 0.004	393.8170	14.481 ± 0.006	393.8177	14.140 ± 0.016
–	–	393.8184	14.466 ± 0.004	393.8192	14.477 ± 0.006	393.8199	14.142 ± 0.016
–	–	397.7000	14.473 ± 0.004	397.6944	14.434 ± 0.006	397.6972	13.910 ± 0.016
–	–	397.7011	14.486 ± 0.005	397.6953	14.440 ± 0.007	397.6980	13.985 ± 0.016
–	–	397.7019	14.492 ± 0.004	397.6961	14.415 ± 0.007	397.6987	14.006 ± 0.017
–	–	398.6916	14.168 ± 0.004	397.7174	14.487 ± 0.009	398.6887	13.661 ± 0.016
–	–	398.6927	14.149 ± 0.004	398.6860	14.128 ± 0.007	398.6894	13.574 ± 0.016
–	–	398.6937	14.171 ± 0.004	398.6871	14.131 ± 0.005	398.6901	13.599 ± 0.015
–	–	405.6867	14.098 ± 0.005	398.6878	14.112 ± 0.007	405.6884	13.532 ± 0.016
–	–	405.6891	14.062 ± 0.004	405.6877	13.949 ± 0.005	405.6908	13.478 ± 0.015
–	–	405.6915	14.061 ± 0.004	405.6901	13.976 ± 0.004	405.6932	13.471 ± 0.015
–	–	405.6939	14.077 ± 0.004	405.6925	13.948 ± 0.005	405.6956	13.494 ± 0.015
–	–	405.6963	14.064 ± 0.004	405.6948	13.952 ± 0.005	405.6979	13.474 ± 0.015
–	–	405.6987	14.063 ± 0.005	405.6972	13.978 ± 0.005	405.7003	13.490 ± 0.015
–	–	405.7011	14.062 ± 0.004	405.6996	13.931 ± 0.006	405.7027	13.473 ± 0.016
–	–	405.7035	14.071 ± 0.004	405.7020	13.926 ± 0.006	405.7051	13.476 ± 0.016
–	–	405.7059	14.081 ± 0.004	405.7044	13.959 ± 0.006	405.7075	13.433 ± 0.015
–	–	405.7083	14.073 ± 0.004	405.7068	13.963 ± 0.006	405.7099	13.489 ± 0.015
–	–	407.7967	14.084 ± 0.005	405.7092	13.960 ± 0.006	407.7982	13.513 ± 0.015
–	–	407.7989	14.084 ± 0.004	407.7976	13.987 ± 0.007	407.8004	13.496 ± 0.016
–	–	407.8011	14.106 ± 0.004	407.7998	13.995 ± 0.007	407.8026	13.522 ± 0.017
–	–	407.8033	14.106 ± 0.004	407.8020	14.002 ± 0.008	411.7116	13.645 ± 0.017
–	–	411.7094	14.217 ± 0.004	411.7106	14.090 ± 0.008	411.7146	13.597 ± 0.016
–	–	411.7127	14.298 ± 0.005	411.7138	14.136 ± 0.008	411.7181	13.719 ± 0.019
–	–	411.7154	14.200 ± 0.004	411.7173	14.089 ± 0.009	417.6825	14.003 ± 0.019
–	–	417.6803	14.490 ± 0.004	417.6847	14.467 ± 0.015	417.6857	13.952 ± 0.021
–	–	417.6836	14.447 ± 0.004	417.6880	14.305 ± 0.017	417.6897	14.057 ± 0.018
–	–	417.6868	14.539 ± 0.004	417.6889	14.452 ± 0.018	417.6928	14.010 ± 0.016
–	–	417.6908	14.415 ± 0.005	417.6919	14.416 ± 0.009	420.6790	14.064 ± 0.017
–	–	420.6775	14.643 ± 0.004	420.6783	14.575 ± 0.007	420.6812	14.091 ± 0.016
–	–	420.6797	14.612 ± 0.004	420.6805	14.514 ± 0.009	420.6834	14.143 ± 0.018
–	–	420.6819	14.549 ± 0.004	420.6827	14.591 ± 0.008	420.6856	14.100 ± 0.017
–	–	420.6841	14.595 ± 0.004	420.6850	14.571 ± 0.010	–	–

Note: *Date = MJD - 58000 in days
Note: Effective wavelength for the R filter, λ_{eff} = 634.9 nm.